Aerospace Science and Technology 153 (2024) 109411

Contents lists available at ScienceDirect

Aerospace Science and Technology

journal homepage: www.elsevier.com/locate/aescte

Aerodynamic and aeroacoustic design of electric ducted fans

Fabio Casagrande Hirono [a,*], Antonio J. Torija [a], Sam D. Grimshaw [b], Dominic Cousins [b], Judith Farman [b], James V. Taylor [b]

[a] School of Science, Engineering and Environment, University of Salford, Manchester, M5 4WT, United Kingdom
[b] Whittle Laboratory, University of Cambridge, Cambridge, CB3 0DY, United Kingdom

ARTICLE INFO

Communicated by Mehdi Ghoreyshi

Keywords:
Electric ducted fan
Aerodynamics
Aeroacoustics
Psychoacoustics

ABSTRACT

This paper describes the aerodynamic and aeroacoustic design of an electric ducted fan (EDF). A prototype EDF was designed and built with three different rotor-stator sets to operate at design flow coefficients $\phi_d = [0.60, 0.75, 0.90]$. Computational Fluid Dynamics (CFD) simulations show that changing the design flow coefficient changes the proportions of endwall and blade profile loss, with the $\phi_d = 0.75$ design providing the optimum balance. CFD predictions of aerodynamic performance are compared with experimental measurements and show good agreement. Data collected from full annulus Unsteady Reynolds-Averaged Navier Stokes (URANS) CFD simulations is used to predict tonal noise radiation using a numerical solution to Farassat's Formulation 1A, and compare favourably to acoustic measurements in an anechoic chamber. All three EDF iterations show similar levels of broadband noise radiation, although tonal noise radiation decreases with increasing design flow coefficient and results in more favourable Sound Quality Metrics performance. Design flow coefficient is shown to have a first-order impact on both the aerodynamic and aeroacoustic behaviour of the EDF, and it is proposed that an optimal design, encompassing both aerodynamic performance and reduced acoustic impact, can be achieved at design flow coefficients between $\phi_d = 0.75$ and $\phi_d = 0.90$.

1. Introduction

The design of electric aircraft is an emerging field, important for decarbonising short-haul passenger transport [1,2]. Many electric aircraft concepts and prototypes have chosen electric ducted fans (EDFs) for propulsion. In these applications the requirement to operate close to and within city centres, the use of novel aircraft architectures, and strict regulatory and societal demands, have favoured the use of ducted fans [3]. This paper aims to establish a methodology for EDF design, show that acoustic predictions using unsteady computational fluid dynamics (CFD) can inform design choices, and provide guidance on how to maximise EDF aeroacoustic performance.

In previous work, the authors of this paper reported the aerodynamic design and aeroacoustic testing of an initial prototype EDF within the same project [4]. This prototype contained three blade rows: inlet guide vanes (IGVs), rotors, and stators, and was designed, built and tested so that aerodynamic, aeroacoustic and psychoacoustic metrics could be reported. The study found that broadband noise dominated the acoustic far-field and increased with increasing rotation rates. It is also shown that the sound quality metrics, Zwicker's Psychoacoustic Annoyance and Loudness, increased with greater rotational speed, while Tonality and Sharpness had more complex variations in directivity patterns across rotational frequencies.

The goal of this paper is to report the next iteration of EDF design and to show how competing objectives across different engineering disciplines can be traded to improve overall performance. Its novelty lies in bringing together aerodynamic, acoustic and psychoacoustic experimental and numerical work to find optimal EDF design points for maximum performance and minimum noise impact. The design methodology reported in [4] is extended to include off-design performance and CFD modelling and in a step towards full acoustic prediction capabilities, unsteady CFD data is used to predict tonal noise radiated from the propulsor. Model predictions are compared with experimental measurements performed in a wind tunnel at the Whittle Laboratory, University of Cambridge, and in an anechoic chamber at the Acoustics Research Centre, University of Salford.

* Corresponding author.
E-mail addresses: fchirono@gmail.com (F. Casagrande Hirono), A.J.TorijaMartinez@salford.ac.uk (A.J. Torija), sdg33@cam.ac.uk (S.D. Grimshaw), drc60@cam.ac.uk (D. Cousins), jrf55@cam.ac.uk (J. Farman), jvt24@cam.ac.uk (J.V. Taylor).

https://doi.org/10.1016/j.ast.2024.109411
Received 21 March 2024; Received in revised form 11 July 2024; Accepted 18 July 2024
Available online 26 July 2024

Nomenclature

A	surface area	m^2
AR	aspect ratio	
C_T	thrust coefficient	
C_P	power coefficient	
C_{ps}	static pressure coefficient	
C_{ptt}	total-to-total pressure coefficient	
C	blade chord [m], constant motor loss coefficient	
D	diameter	m
DF	diffusion factor	
I	motor current	A
J	advance ratio	
M_{tip}	tip Mach number	
N	blade count	
P_{loss}	motor power losses	W
R	microphone arc radius	m
S	blade pitch	
T	thrust	N
U	rotor blade speed	m/s
V	velocity	m/s
X_{ND}	non-dimensional axial position	
f_s	sampling frequency	Hz
f_{shaft}	shaft frequency	Hz
h	static specific enthalpy	J
k	$\tan(\alpha_{2,rel})$, motor loss coefficients	
$\dot{m}$	mass flow rate	kg/s
n	vortex design exponent	
p_0	stagnation pressure	Pa
p_s	static pressure	Pa
r	radius	m
v	axial velocity	m/s
y^+	wall normal boundary layer resolution	
α	swirl angle	°
ϵ	jet speed ratio	
η_{poly}	polytropic efficiency	
θ	acoustic emission angle	°
ρ	air density, material density	kg/m^3
σ	duct area ratio, mechanical stress	
ϕ	flow coefficient	
χ	blade metal angle	°
ψ	stage loading coefficient	
ω	rotational speed	rad/s

Subscripts

$0, \ldots, 4$	control volume stations
c	casing, motor copper
i	motor iron
dwn	down
d	design point
h	hub
m	meanline
pr	flow probe
r	rotor
s	stator
up	up
w	motor windage
x	axial direction
θ	circumferential direction

(a) $\phi_d = 0.60$ (b) $\phi_d = 0.75$ (c) $\phi_d = 0.90$

Fig. 1. Three rotor-stator blade sets with varying design point flow coefficients: the nacelle and hub are shown in grey, the rotor blades are shown in blue, and the stator vanes are shown in red. (For interpretation of the colours in the figure(s), the reader is referred to the web version of this article.)

An updated EDF layout with rotor and stator blade rows is adopted and the design flow coefficient, $\phi_d = V_x/U_m$, varied to create the three blade sets shown in Fig. 1. These three designs share the same nacelle and hub geometry and all meet the same mission requirements, i.e. thrust, flight speed and altitude at stationary, take-off and cruise conditions. Design flow coefficient is critical for EDF design as it has a first order effect on all of the major performance metrics: Aerodynamic losses are controlled by changes in the flow velocity triangles through the rotor and stator rows, the rotation speed and torque, which are set by flow coefficient, determine the design and performance of the electrical and structural aspects of the EDF, and acoustic performance is affected by rotation and blade passing frequencies, as well as the aerodynamic loading.

The EDF designed, manufactured and tested in this study is powered with a brushless DC electric motor and produces 5 kg of static thrust and 1.5 kg of thrust when cruising at 30 m/s. It has a blade tip diameter of 120 mm, 1/9th the size of the full-scale EDF developed by the Project InCEPTion consortium led by Greenjets Ltd.[1]

The paper is divided into seven sections. After the introduction, the second section provides a literature review covering the aerodynamic design of EDFs and their acoustic behaviour. The third section presents design, simulation and experimental methods and the fourth section details the aerodynamic performance of the three different blade designs using computational fluid dynamics (CFD) and experimental results. The fifth section compares acoustic predictions with test data collected in an anechoic chamber and the sixth section considers psychoacoustics and multi-disciplinary design, before the final section provides the conclusions.

[1] URL. https://www.gov.uk/government/news/84-million-boost-for-technology-to-power-a-green-aviation-revolution

2. Literature review

2.1. Ducted fan aerodynamics

Research on ducted fans has been carried out since the 1930s. Extensive work has gone into their use in turbofan engines for commercial, transonic flight and an up-to-date review of this technology is carried out by Benini et al. [5]. An overview of ducted fan design and testing for static and low-speed flight is presented by Zhang and Barakos [6] who split the research into two distinct groups: large scale experimental campaigns carried out in the 1950s and 60s for human-flight applications, and more recent lab-based tests related to unmanned aerial vehicles. In both groups, machines with low blade counts, 6 or fewer, are most common and in some cases these are designed as propellers and tested with and without ducts. Zhang and Barakos highlight six research challenges: cross-wind effects, tip clearance, high-speed performance, noise emission, control systems and coaxial (contra-rotating) ducted fan systems. The authors do not comment how these topics are interconnected and do not consider turbomachinery design, off-design performance or matching between aerodynamic and electrical components in their discussion.

Bacchini et al. [7] compare the performance of different electric Vertical Take-Off and Landing (eVTOL) propulsor architectures, concluding that the optimal design is mission-dependent. For short-range missions, the high hovering efficiency of multi-rotor designs proves to be the most effective, while longer range missions with higher cruise duration require vectored-jet type architectures and remain out of reach of multi-rotor configurations. The lift and cruise propulsor arrangement provides a compromise between the two. Bacchini et al.'s work highlights the importance of designing efficient propulsion systems for a range of flight conditions, i.e. varying flight speed and thrust requirements, though does not go into detail about how this should be done.

A technical white paper published by Lilium [3] describes a ducted fan propulsion system using a one-dimensional (1D) meanline, turbomachinery-based approach, where the design flow coefficient is high, $\phi_d > 1.00$, and a variable geometry nozzle gives exit duct area ratios, $\sigma = 0.9 - 1.3$. Weintraub et al. [8] describe the design of a ducted fan using 1D and two-dimensional (2D) turbomachinery design methods including analytical models for loss and off-design performance. The exit duct area ratio is $\sigma = 0.9$ and the flow coefficient can be calculated from the dimensional data as approximately $\phi = 0.8$. Weintraub et al. investigate the effect of varying design parameters: fan diameter and speed, blade aspect ratio and pitch-to-chord ratio, and their effect is evaluated from analytical models; no CFD simulations or experimental tests are provided. Hine et al. [9] present an approach for developing integrated stator-diffusers with short axial lengths with the objective of increasing hover performance whilst minimising propulsor length and weight. This study features CFD design and experimental validation of several stator-diffuser geometries, but does not include results from a fully integrated ducted fan.

Jedamski et al. [10] compare optimised ducted fan and open rotor propulsion systems for a future regional air mobility (RAM) aircraft with distributed propulsion. A 1D model couples meanline calculations with a "cascade solver", duct loss model and "bottom up" weight analysis so that duct design can be optimised for shaft power at cruise and system weight. The results show an improvement in efficiency and weight as the number of propulsors is increased and at a cruise Mach number of 0.39 ducted fans are shown to outperform optimised open rotor systems. The FUN3D CFD code is used to analyse propulsor airframe integration, however, the rotor and stator blades are represented by actuator discs in these calculations so the 1D model is not validated against CFD or experiments in the paper.

The tools used by Jedamski et al. [10] are proprietary and limited information is provided. It is not clear how off-design performance, including stall margin, is included in the analysis and the inclusion of a variable exit duct is mentioned but not explained. The solver uses a cascade model so is assumed not to include three-dimensional loss mechanisms including blade corner separations and over-shroud leakage, and no mention is made of the effect of Reynolds Number as the propulsor size is varied. The designs are optimised based on shaft power so this neglects the effect of motor size on efficiency, although in another paper by Moore et al. [11], the same team explain that multiple small motors are easier to cool than a single large motor. Finally, acoustic performance is considered via variation in blade incidence as a proxy for unsteady blade loading; the lack of turbomachinery CFD means that coupled aero-acoustic calculations are not possible.

2.2. Ducted fan aeroacoustics

2.2.1. Aeroacoustic predictions

This work uses a hybrid approach to predict the tonal noise from the EDF. In a hybrid approach, the acoustic source terms are computed separately from the sound propagation to the far-field. The sound source modelling can include complex geometries and use well-established CFD solvers, and is followed by a fast propagation operator such as Farassat's Formulation 1A (F1A) solution [12] to the Ffowcs Williams-Hawkings (FW-H) acoustic analogy [13]. Hybrid methods do not rely on simplifying assumptions on the geometry and flow as in analytical approaches, and avoid the prohibitive computational cost of direct numerical methods [14,15]. Hybrid approaches are becoming popular for eVTOL propulsor noise predictions [16,17], in part due to the availability of stable computational implementations of Farassat's Formulation 1A, such as PSU-WOPWOP [18].

The Ffowcs Williams-Hawkings equation can be used in two forms, depending on the type of "data surface" used in the CFD calculation: for a data surface that coincides with the physical solid surfaces, the acoustic predictions use the static pressure observed on these surfaces; and for a permeable data surface that encompasses the entire source region, the acoustic predictions use the densities, momentum vectors, and pressures observed on and through the surfaces [19]. Although the solid surface formulation is simpler and faster to run, permeable surface formulations are more accurate for problems involving acoustic shielding and when working with complex geometries [20,21], and therefore are the form chosen in the present work.

2.2.2. Aeroacoustic measurements

There are not many experimental results in the literature on the aeroacoustics of EDFs. Moreau et al. [22] obtained good agreement between direct acoustic computation and measurements of both tonal and broadband noise from a low solidity ducted fan stage for Urban Air Mobility applications, and suggest that most of the noise is generated at the blade tips.

Recent experimental work on propeller aeroacoustics have reported increased broadband noise level and tone broadening when the propeller is operated within a duct at static conditions, versus without the duct [23,24]. Drastic changes in acoustic directivity and spectra were observed, and increased broadband noise levels are hypothesized to originate from the propeller tip vortices interacting with the duct wall and dissipating into incoherent turbulence [23,24]. It was also suggested in some cases the duct can confine the blade-tip vortices, leading to stronger blade-vortex interaction and increased tonal noise at static conditions [24]. Malgoezar et al. [23] reported very similar acoustic spectra with and without the duct when a low-speed incoming airflow was present, possibly due to reduced interaction as the turbulent structures are convected with the mean flow. It has also been proposed that tonal noise radiation of a ducted propeller at the blade passing frequency (BPF) is the result of interference between the upstream and downstream acoustic radiation, and can be minimized by centring the propeller axially within the duct [25].

The aeroacoustics literature indicates that the dominant sources of noise in ducted fans are always 3D in nature and therefore the hybrid

Table 1
Meanline design for the three different EDF designs.

Design flow coefficient, ϕ_d	0.60	0.75	0.90
Rotor blade count, N_{rotor}	7	8	11
Stator blade count, N_{stator}	6	9	15
Rotational speed (rpm) @ 8 N thrust	8023	6464	5642
Blade passing frequency (Hz)	936	862	1034
Duct area ratio, σ	1.0		
Jet area (m^2), A_4	0.0034		
Rotor inlet area (m^2), A_1	0.0034		
Hub radius (m), r_h	0.025		
Rotor tip radius (m), r_c	0.070		
Mean line radius (m), r_m	0.053		

numerical approach used in this paper is appropriate. However, the literature also shows that there is limited work on how the preliminary and detailed design of EDF blades determine the acoustic performance of the propulsion system.

Overall, this literature review highlights that in certain applications EDF propulsion systems can provide efficiency and acoustic performance gains over open rotor designs. There is a lack of detailed CFD simulation results and up-to-date experimental testing, limited information on how to design for a range of operating points, and little discussion on how to trade or match aerodynamic, electrical, mechanical and acoustic performance. This paper seeks to address these questions by providing an integrated approach to design, manufacture and testing of EDFs. It also appears that this paper is the first to investigate the coupled aerodynamic and psychoacoustic performance of different designs.

3. Methodology

Numerical and experimental approaches are used for both aerodynamic and aeroacoustic analysis and these are described in two subsections: the first presents the aerodynamic design, including a low-order inverse design tool for creating meanline and 2D rotor and stator geometries to achieve a required thrust target. The second subsection describes the methods used to analyse the performance of the ducted fans. This includes CFD simulations, acoustic predictions, the manufacture of the three ducted fans, and experimental wind tunnel and anechoic chamber measurements.

3.1. Aerodynamic design

Three sets of rotor and stator blades are investigated, denoted by their design point flow coefficient $\phi_d = [0.60, 0.75, 0.90]$. These rotor-stator sets offer varying degrees of aerodynamic performance, with higher flow coefficient designs achieving greater thrust for a given rotation speed, as indicated in Table 1. Blades counts differ for each set and overall it is not straightforward to determine *a priori* which set offers the best balance of aerodynamic, aeroacoustic and psychoacoustic performance.

3.1.1. Low-order inverse design

The low order inverse design tool takes a set of dimensional and non-dimensional input parameters and uses mean flow and two-dimensional calculations to produce preliminary geometries for the rotor and stator blades.

Design begins by specifying a set of required thrusts, flight speeds and altitudes with which the EDF is intended to operate. At this stage the rotor tip diameter of the EDF is also fixed, though this decision can be iterated if required. The hub diameter is set by the motor selection, and a meanline radius with equal area above and below is defined as

$$r_m = \sqrt{\frac{r_h^2 + r_c^2}{2}}, \tag{1}$$

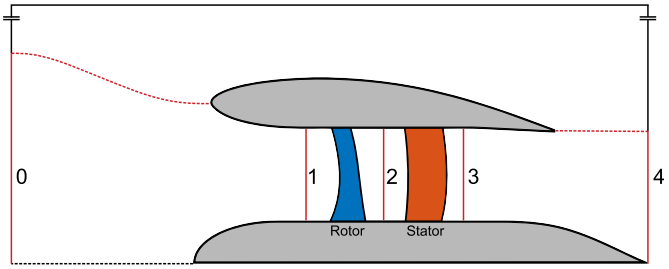

Fig. 2. Ducted fan control volume.

where r_h and r_c are the hub and tip radii respectively.

Analysis of the control volume in Fig. 2 using the steady flow momentum equation relates thrust to flight speed, jet velocity, jet area and the static density of the air

$$T = \dot{m}(v_4 - v_0) = \rho A_4 v_4 (v_4 - v_0). \tag{2}$$

Thrust can then be non-dimensionalised and expressed as a function of the flight speed to jet velocity ratio, ϵ

$$C_T = \frac{T}{\rho A_4 v_4^2} = 1 - \frac{v_0}{v_4} = 1 - \epsilon. \tag{3}$$

The steady flow energy equation is used to calculate the power transferred to the flow assuming isentropic processes and can be similarly non-dimensionalised as

$$C_P = \frac{\Delta h_0}{\rho A_4 v_4^3} = \frac{1 - \epsilon^2}{2}. \tag{4}$$

Rotation speed is related to the control volume analysis via the flow coefficient, $\phi = v_1 / U_m$, which is the ratio of meanline rotor inlet velocity to meanline blade speed. The EDF in the current work operates at low speeds so its flow is assumed incompressible, therefore the jet velocity and rotor inlet velocity are related by

$$\frac{v_1}{v_4} = \frac{A_4}{A_1} = \sigma. \tag{5}$$

Specifying the duct area ratio, σ, and the design flow coefficient, ϕ_d, sets the meanline blade speed and rotation rate so that the meanline design is fixed for a given set of input parameters at a single operating point. In this study, the effect of varying design flow coefficient is investigated while duct area ratio is kept constant at $\sigma = 1$. Further work should be performed to examine the effect of duct area ratio on aerodynamic and psychoacoustic performance.

3.1.2. Off-design operation

To analyse the performance of the EDF at other operating points, the fan stage loading coefficient is derived using Euler's work equation while specifying zero swirl, i.e. no IGVs, at inlet to the rotor

$$\psi = \frac{\Delta h_0}{U_m^2} = \frac{v_{\theta 2}}{U_m} = 1 + k\phi, \tag{6}$$

where $k = \tan(\alpha_{2,rel})$ and $\alpha_{2,rel}$ is the swirl angle in the rotor frame of reference downstream of the rotor row. To calculate the meanline off-design performance of the EDF, the deviation angle of the flow leaving the rotor is assumed constant so that $\alpha_{2,rel}$ and k are constant at the value fixed by the blade design. The stagnation enthalpy rise through the rotor is then matched to the control volume analysis by equating Δh_0 in Equations (4) and (6), yielding

$$\frac{\phi^2}{2\sigma^2}(1 - \epsilon^2) = 1 + k\phi. \tag{7}$$

For a specified off-design operating point, ϵ is known so Equation (7) can be rearranged to solve for ϕ:

Table 2
Operating points for the EDF designs.

Operating point	Thrust (N)	Flight Speed (m/s)	Altitude (m)	Air density (kg/m^3)
Take-off (Design point)	30	20	0	1.22
Static	50	0	0	1.22
Cruise	20	40	3000	0.91

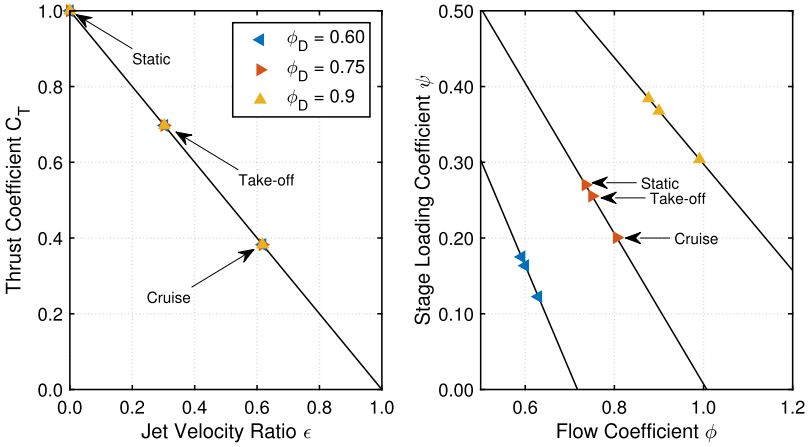

Fig. 3. Non-dimensional operating points of the three turbomachinery designs.

$$\phi = \frac{k\sigma^2 + \sigma\sqrt{k^2\sigma^2 + 2(1-\epsilon^2)}}{1-\epsilon^2}. \tag{8}$$

Table 2 gives the dimensional propulsor requirements for three flight conditions while Fig. 3 shows the ideal (isentropic, constant deviation) non-dimensional operating points that are achieved. It shows thrust coefficient, C_T, against flight speed to jet speed ratio, ϵ, and stage loading coefficient, ψ, against flow coefficient, ϕ.

Fig. 3(a) characterises the operating point of the EDF in terms of "external" variables, i.e. the thrust, air properties, flight speed, and jet area and speed, which are independent of the blade designs. This is in contrast to the advance ratio, $J = v_0/U_m$, which depends on both the external flow and the internal blade design. Using ϵ instead of J has the advantage of decoupling the external and internal flows.

Fig. 3(b) characterises the operating point of the EDF blade rows. At this point in the design, isentropic flow is assumed so efficiency cannot be evaluated. However, the size of the variation in ideal flow coefficient and stage loading coefficient gives a first indication of the operating range required from the fixed geometry fan stage and the design operating point can be adjusted to sit in the middle of this range. This helps to provide adequate stall margin for the operating point with lowest flow coefficient, and good efficiency across the EDF's entire operating range. The fan pressure rise characteristic, including efficiency and stall point, is updated once the blade geometry is generated and 3D Reynolds-Averaged-Navier-Stokes (RANS) CFD used to simulate candidate designs.

3.1.3. Velocity triangles

After the meanline design is fixed at rotor and stator inlet and outlet, at Stations 1, 2 and 3 shown in Fig. 2, it is necessary to design the variation in velocity triangles between the hub and casing. This is achieved by solving the simple radial equilibrium equation (SRE) numerically.

$$\frac{dh_0}{dr} = v_x\frac{dv_x}{dr} + \frac{v_\theta}{r}\frac{d(rv_\theta)}{dr}. \tag{9}$$

Upstream of the rotors, $v_{\theta 1} = 0$ and the enthalpy is uniform across the span, therefore the axial velocity is constant. Work is added to the flow by the rotor and thus a further equation is required to determine the spanwise distribution of the flow quantities. Using Euler's work equation derived in Dixon and Hall [26] the variation in stage loading can be written as

$$\Psi = \frac{\Delta h_0}{U^2} = \frac{(v_{\theta 2} - v_{\theta 1})}{\omega r} = \Psi_m\left(\frac{r_m}{r}\right)^{n+1}, \tag{10}$$

where n, the "vortex design exponent", is an aerodynamic input parameter for the low order design tool. This sets the distribution of circumferential velocity at Station 2, downstream of the rotor, and along with the stagnation enthalpy distribution here, Equation (9) can be solved numerically to find the axial velocity distribution.

At Station 3 the circumferential velocity is zero, and as the stator causes no change in stagnation enthalpy it is the same as at Station 2. Again Equation (9) is solved numerically to finalise the velocity triangles.

For all three designs, the vortex design exponent is chosen as $n = 0.5$, closer to a free-vortex than a forced-vortex design. The distributions of the swirl angle and flow coefficient downstream of the rotor are shown in Fig. 4. As the meanline design flow coefficient is increased the quantity of turning required by the rotor in the absolute frame increases across the entire span and the swing in flow coefficient between the hub and casing ends of the blades is reduced.

3.1.4. Blade loading and deviation correlations

The next step is to design blades which achieve the flow specified by the velocity triangle analysis. This is accomplished using two well established correlations: Lieblein's [27] Diffusion Factor (DF) and Howell & Carter's [28] rules for deviation. Lieblein [27] reported the correlation shown in Equation (11) which relates mean-line pitch-to-chord ratio to diffusion factor, a measure of flow deceleration and hence pressure rise towards the trailing edge. To limit the likelihood of separation, Lieblein recommended $DF < 0.6$. In this preliminary design tool the blade aspect ratio is specified as an input parameter based on manufacturing and mechanical constraints, and the meanline chord is therefore specified by the geometric inputs. Given the chord, the upstream and downstream flow velocities, and a maximum specified diffusion factor, the blade pitch is calculated from Equation (11). The blade count is then calculated from the pitch and rounded up to the nearest integer. Finally, the meanline pitch is recalculated for the integer number of blades.

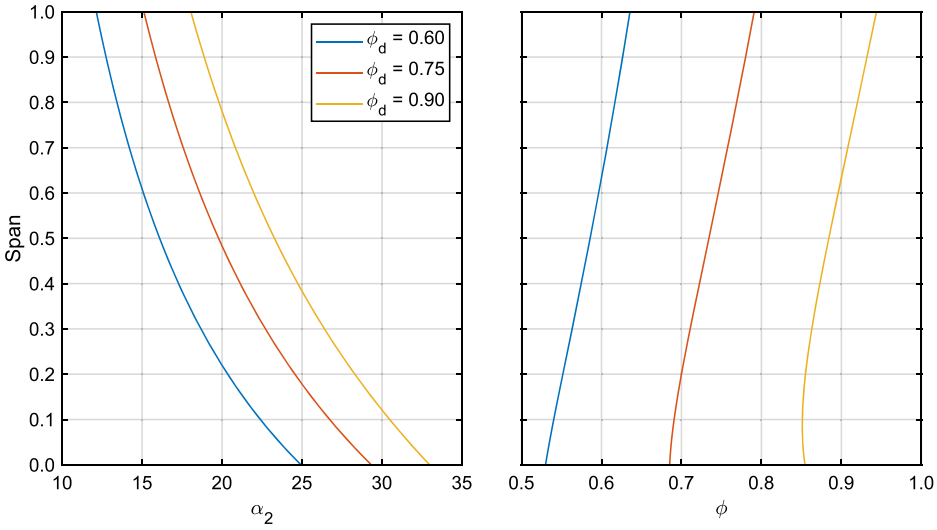

Fig. 4. Comparison of spanwise distributions of swirl angle and flow coefficient downstream of rotor for the three different EDF designs.

$$DF \approx 1 - \frac{v_{dwn}}{v_{up}} + \frac{\Delta v_\theta}{2v_{up}} \frac{S_m}{C_m}. \tag{11}$$

The blades are formed from subsonic controlled diffusion type aerofoils created using a camberline and thickness with the shape transform described by Kulfan [29]. These sections are mapped onto the inlet and outlet metal angles. Inlet angles are set so that the blades run with zero incidence at the design point. Outlet angles are calculated using an empirical correlation presented by Howell & Carter [28] that predicts flow deviation from the blade trailing edge. Their correlation has been rearranged in Equation (12) to give an expression for exit blade metal angle at meanline radius, and this is evaluated using previously calculated flow angles and the pitch-to-chord ratio.

$$\chi_{dwn} = \frac{\alpha_{dwn} - M\chi_{up}\sqrt{S/C}}{1 - M\sqrt{S/C}}, \quad \text{where} \quad M = 0.23 + 0.002\alpha_{dwn}. \tag{12}$$

To calculate the chord and downstream metal angle distributions across the span, the deviation ($\alpha_{dwn} - \chi_{dwn}$) is set to the mean-line radius value. The chord is then set by rearranging and solving Equation (12). This means the diffusion factor, given in Equation (11), changes across the span, and the highest diffusion factor may not be at the meanline radius where it is specified. An iterative loop is implemented to set a meanline diffusion factor which ensures the maximum diffusion factor limit is not exceeded.

In these three designs the meanline diffusion factor is set to $DF = 0.4$, the rotor aspect ratio $AR_r = 2.5$ and the stator aspect ratio $AR_s = 2.2$. This results in the spanwise distributions of diffusion factor shown in Fig. 5 and the blade counts in Table 1.

3.1.5. Nacelle geometry and 3D blade design

The nacelle, nose bullet and tail cone geometry are specified using a shape transform [29] and are designed using steady, 3D CFD calculations, where the shape transform parameters are updated iteratively to minimise adverse pressure gradients at both static and cruise operating conditions. The nacelle is relatively thick compared to conventional aero engines as the full-size demonstrator designed for Project InCEPTion must house electrical and cooling equipment. The effect on overall drag is minimal, as the flight velocities are subsonic and the flow remains attached to the rear of the nacelle.

Results from steady CFD simulations are also used to modify the initial blade geometry to correct for simplifications made within the preliminary design; these include the assumption of no spanwise loss variation and the use of correlations for blade loading and deviation. The inlet and exit blade metal angles are adjusted to match the design velocity triangles and the chord distribution is modified to achieve constant deviation across the span.

A key aspect of any EDF design is that it operates efficiently at a wide range of operating points. As the fan is low speed and the nozzle is unchoked, any changes in flight velocity to jet velocity ratio ϵ result in a change in fan flow coefficient ϕ as shown in Fig. 3. It is essential that the fan has enough margin to operate at the static condition without stalling, and that the efficiency at this operating point is also high to reduce the peak absolute power requirement on the system. To address these challenges, 3D blade design, specifically compound sweep and lean, is included to extend the operating range of the EDF by preventing the formation of open corner separations [30].

3.2. Aerodynamic and acoustic simulation and measurement

3.2.1. Steady and unsteady aerodynamic simulations

CFD simulations are performed using the 3D structured multiblock RANS code TURBOSTREAM[2] with the Spallart-Allmaras turbulence model [31]. The solver is validated on a number of different turbomachinery cases in [32]. Blade passage meshes are created in AUTOGRID[3] and the mesh around the nacelle and in the farfield is created using MATLAB.[4] The walls are resolved with a $y^+ < 1$ and the farfield domain extends eight tip radii in all directions.

This results in a domain with approximately 3 million cells for single passage calculations of the two blade rows plus farfield. These steady calculations are used for design purposes as they are relatively quick to run, completing in one hour on a single Nvidia A100 GPU. The domain is shown in Fig. 6, upstream and around the EDF a farfield type boundary condition is used, this allows the flow direction to float depending on what is demanded by the cells internal to the calculation. It can also have flow crossing it in either direction: if the flow is inwards, the stagnation pressure and temperature are used, if the flow is exiting the static pressure is used. Downstream of the EDF a standard static pressure outlet boundary condition is used.

Unsteady CFD simulations are used to provide inputs into the acoustic simulations. In this case it is necessary to use the time-accurate formulation of TURBOSTREAM that uses the dual timestepping method of Jameson [33] to solve the flow. The domain is repeated circumferentially to construct a full annulus domain with interpolating patches between the stationary and rotating frames, which substantially increases

[2] URL. https://www.turbostream-cfd.com/
[3] URL. https://www.numeca.com/product/omnis-autogrid
[4] URL. https://uk.mathworks.com/products/matlab.html

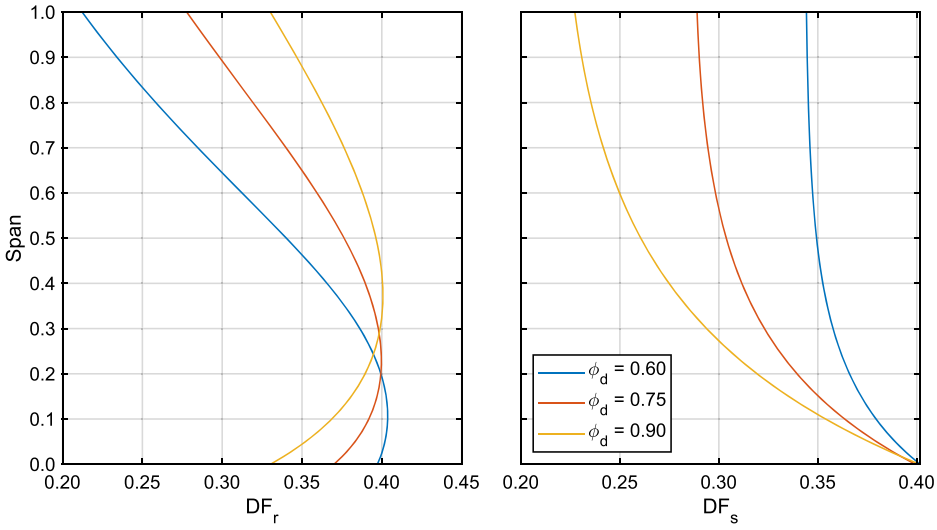

Fig. 5. Comparison of spanwise distributions of diffusion factor for rotor and stator blades for the three different EDF designs.

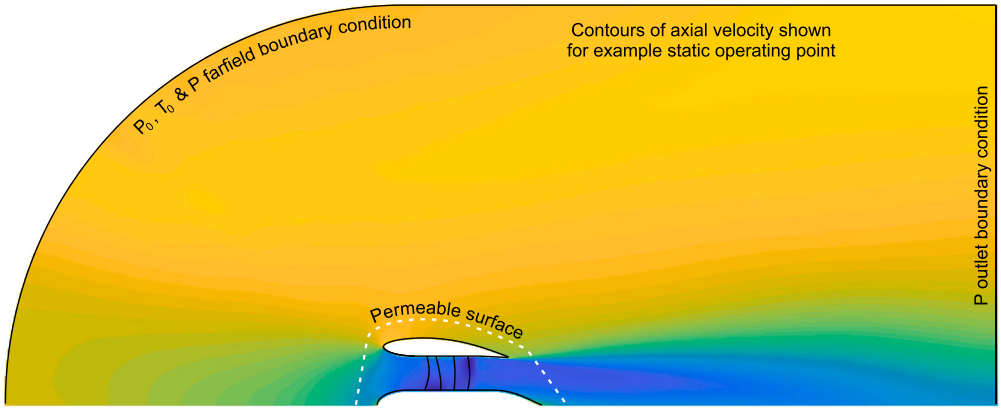

Fig. 6. Circumferential average of coupled nacelle and blade row CFD simulation of EDF, showing domain boundaries and permeable surface for output of time series data.

the cell count of the calculation. Because the blade counts vary between the different designs, the mesh count also varies; as an example, the $\phi_d = 0.75$ has approximately 24 million cells. These calculations take around 18 hours to complete 12 revolutions of the EDF when run on four Nvida A100 GPUs. The calculations are run for 24 revolutions to flush transients before logging the production data.

3.2.2. Acoustic predictions using farassat F1A

Acoustic predictions are performed using the unsteady CFD data as input to PSU-WOPWOP [18]. CFD data is output on the permeable surface shown in Fig. 6 for a single blade passing covered by 100 timesteps at the end of the CFD calculation. The values of time-varying pressure, density and velocity surrounding the EDF are written to file by the CFD solver and this data is converted to PSU-WOPWOP input files using an open-source Python program written specifically for this project, `pywopwop`.[5] A periodic PSU-WOPWOP input file is created, allowing the prediction of tonal noise. The simulation includes an arc of observers around the EDF, emulating the aeroacoustic measurement setup. A separate module within `pywopwop` is then used to read PSU-WOPWOP observer grid output files into Python again for further analysis and plotting of the predicted acoustic pressure signals.

[5] URL. https://github.com/fchirono/pywopwop

3.2.3. Manufacture

The final EDF design was manufactured with a combination of 3D-printed plastic parts and aluminium parts CNC machined from solid. Fig. 7a shows a render of the EDF assembly with the inlet duct and nose bullet hidden. The motor is mounted at the rear of the hub section, supported by the stator blisk, and the rotor is fixed to the rotor shaft with a collet which ensure its axis and the motor are aligned. The power cables are fed out of the hub through the tail cone and a single strut. The rotor requires balancing to ensure smooth running and this was achieved by adding weight to the shroud ring.

A photo of the completed unit is shown in Fig. 7b. The nacelle, IGVs, nose bullet and tail cone are all laser sintered in nylon, this results in relatively tough parts. The nacelle assembly breaks down to three parts to enable the motor and blades to be quickly assembled or disassembled, and these parts are hollow to reduce mass and enable future flight testing. The rotor and stator blades are printed as one-piece blisks using stereolithography 3D printing.

3.2.4. Aerodynamic wind tunnel experiment

This section outlines the experimental methods used to assess the performance of the EDF with different blade designs. The test rig, shown in Fig. 7, consists of a blow-down wind tunnel with a working section instrumented to measure thrust force, power consumption, intake surface pressure distributions and exit jet flow-field properties. When mounted in the working section the EDF causes 4.6% blockage.

(a) Render with inlet hidden (b) Manufactured EDF with pressure taps (c) EDF in wind tunnel

Fig. 7. Render and photographs of manufactured EDF assembly and wind tunnel mounting.

Upstream total and static pressure probes are used to measure the wind tunnel flow velocity. Air density is calculated using measurements of atmospheric pressure and temperature, and EDF net thrust is measured using a calibrated load cell. The load cell signal is amplified, logged over a period of 5 seconds and time averaged. Rotation speed is logged using an optical tachometer mounted in the casing above the rotor shroud, which is used to automatically set the operating point using a servo controller. The EDF is powered by a 44 V DC bench supply from which electrical power consumption is monitored.

The flow field downstream of the propulsor in the exit jet is measured using an automated two-axis traverse system with a calibrated five-hole pneumatic probe. Traverses are taken in a plane a distance of r_c downstream of the duct exit. A probe with a head diameter of $D_{pr} = 2$ mm is used to provide an acceptable compromise between settling time and measurement accuracy for this application, as described by Grimshaw and Taylor [34]. The probe is calibrated over a matrix of pitch and yaw angles from $-26°$ to $26°$ in $2°$ increments at five flow velocities in order to match the Reynolds number of the measured flow. Traverse grid points are clustered at the hub and casing radii. EDF mass flow rate is measured using a calibrated intake static pressure tapping, as described by Dunkley [35]. The tapping is calibrated over a range of values of ϵ to account for changes in intake flow distribution. Total pressure in the exit jet is measured using a Pitot probe positioned at mid span. The true mass-averaged total pressure in the jet is obtained by calibrating the Pitot probe against mass-averaged full annulus traverses. Intake surface pressure distributions are measured using 26 static pressure tappings around the inner and outer surface. Tappings are clustered towards the leading edge where the rate of change of pressure gradient is large to accurately resolve the distribution.

3.2.5. Anechoic chamber aeroacoustic experiment

The measurement setup inside the anechoic chamber is shown in Fig. 8. The EDF is installed on a rotating stand instrumented with a load cell for measuring thrust, and the stand is installed at the centre of the chamber. A fixed microphone arc with ten free-field, 1/2" microphones at $R = 2.5$ m radius is used to measure far-field noise between emission angles $\theta = 0°$ (on-axis, downstream) and 90°, in 10° steps. The stand is then rotated 180° in the azimuthal direction, and the measurement procedure is repeated to cover emission angles between $\theta = 90°$ and 180° (on-axis, upstream). Wind shields are used on the lowest three microphones to attenuate the effects of any incident flow when measuring downstream from the EDF.

All acoustic and non-acoustic sensors are synchronously acquired using Dewesoft[6] data acquisition units and recorded on a personal computer for 30 seconds. The microphones and optical tachometer signals are logged at $f_s = 50$ kHz sampling rate, while the load cell and thermocouple are acquired at $f_{s2} = 12.5$ kHz. A real-time monitoring screen is set up to observe instantaneous values for thrust, temperature, and rotational speed, thus enabling accurate and safe control of the EDF operating conditions.

The three EDF blade designs are operated at a static condition and 8 N mean thrust, which results in different rotational speeds for each blade set as shown in Table 1. These different rotational speeds are expected to affect the aeroacoustic performance, as rotor noise is strongly correlated to rotor blade speed. A more detailed overview of this measurement setup has previously been reported in [4].

3.2.6. Tonal noise extraction

Due to their synthetic nature, the tones obtained from acoustic predictions have a stable rotational frequency, presenting content at integer harmonics of the blade-passing frequency only. However, in an experiment, the motor rotational frequency varies a small amount around its nominal value, resulting in tone broadening. Fig. 9 shows a representative case of instantaneous shaft frequency $f_{\text{shaft}}(t)$ in the time domain, evaluated from the optical tachometer signal and normalised by its mean value $\overline{f_{\text{shaft}}}$, for the $\phi_d = 0.6$ design. Small, random deviations of less than one percent are visible throughout the recording length.

To compensate for these deviations and allow a proper comparison with predictions, the tachometer signal is used to resample the acoustic signals using 512 samples per rotation, phase-locking the acoustic signals with respect to the rotor shaft angle and resulting in a new time series with a stable rotational frequency. This approach is frequently used to analyse acoustic measurements from rotating machines [37–40].

The resampled noise signals are separated into blocks of 4 integer rotations, in order to obtain a high angular frequency resolution. The tonal component of the noise is identical over each block, and is estimated by ensemble averaging the blocks: the stochastic component tends to zero as the number of averaged blocks increases, and the remaining signal component is the tonal, "rotor-locked", or "predictable", component of the noise signal. The stochastic "residual", or "unpredictable", component that is left after subtracting the average from each block is the broadband noise. This approach preserves both amplitudes and phases of the signals, so the measured waveforms can be reconstructed and compared to the predicted waveforms. As the measured rotational frequencies do not show large deviations from their mean values, the resulting angle-domain signals are scaled to the mean measured rotational period, and presented here as conventional time- and frequency-domain signals.

4. Aerodynamic performance

This section presents results quantifying the aerodynamic performance of the EDF with three different blade designs tested with the

[6] URL. https://dewesoft.com/

Fig. 8. Acoustic test setup of EDF in the anechoic chamber [From [36]].

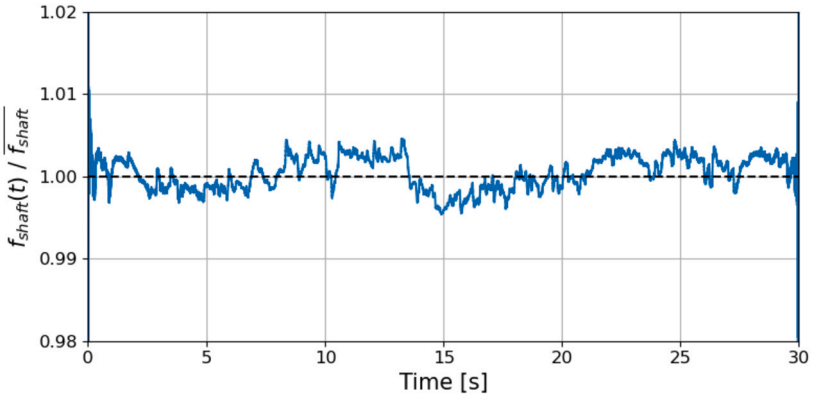

Fig. 9. Instantaneous shaft frequency $f_{\text{shaft}}(t)$ in time domain, normalised by mean shaft frequency $\overline{f_{\text{shaft}}}$.

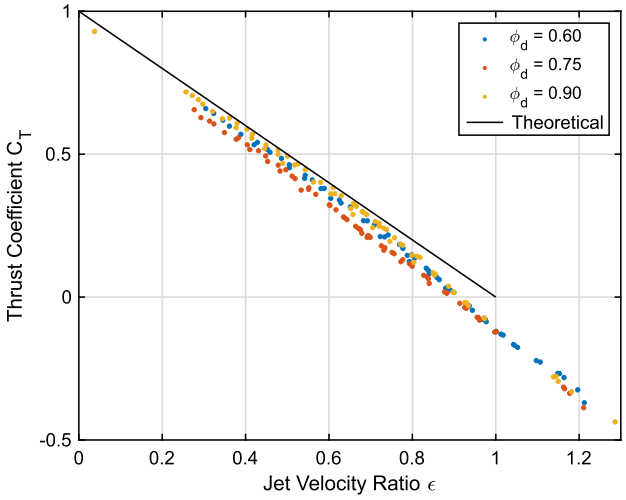

Fig. 10. EDF thrust characteristics derived from experiments run at multiple flight velocities and rotational speeds.

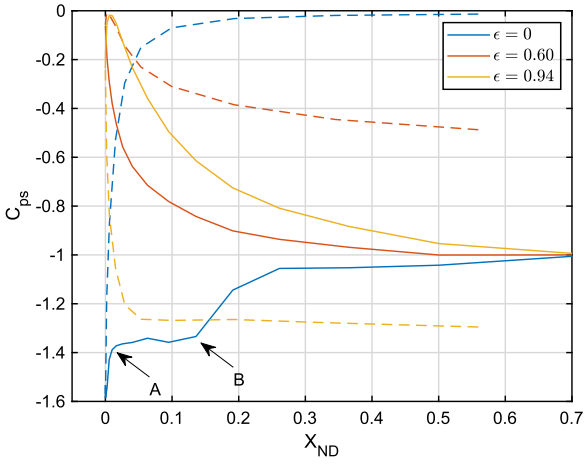

Fig. 11. Intake pressure coefficient distributions for different values of jet velocity ratio, solid line measured on inside of intake, dashed line measured on outside. $\phi_d = 0.6$ blade set.

same motor and nacelle. First, thrust is evaluated in terms of thrust coefficient, C_T and jet velocity ratio, ϵ. Second, intake flow is considered using pressure tapping data and flow visualisation paint. Third, the turbomachinery performance is investigated using measured and com-

(a) Circumferentially-averaged static pressure (b) Circumferentially-averaged stagnation pressure

Fig. 12. Meridional view of flow field through EDF at zero flight speed, $\epsilon = 0$.

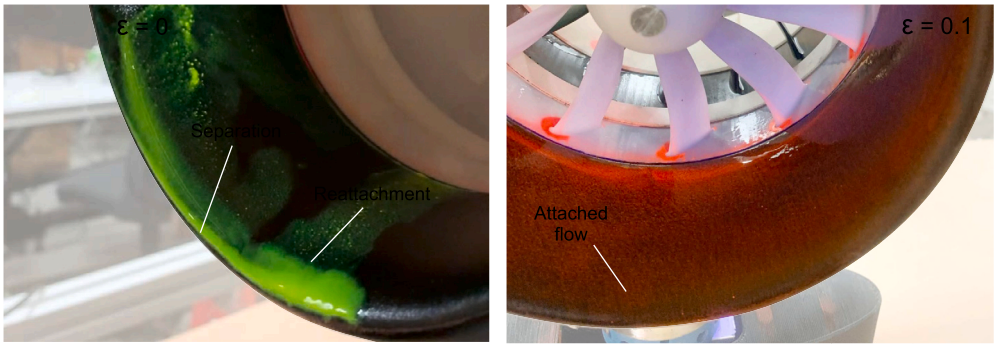

Fig. 13. Intake lip oil flow visualisation to identify inner lip separation at zero flight speed, $\epsilon = 0$.

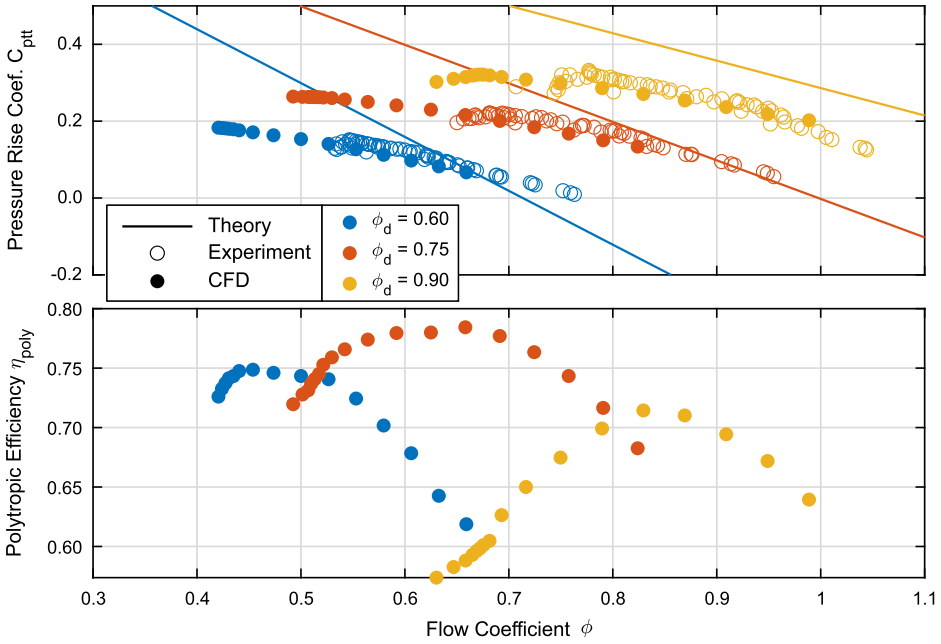

Fig. 14. Comparison of theoretical, computational and experimental fan pressure rise and efficiency characteristics for the three designs.

puted pressure rise characteristics, computed efficiency characteristics, and computed visualisations of the flow through the blade rows.

4.1. Propulsor thrust

Fig. 10 shows C_T plotted against ϵ for the three blade designs tested across a matrix of operating points varying from 500 to 8000 shaft revolutions-per-minute and 5 to 22 m/s wind tunnel speed. The non-dimensionalised results collapse towards a single line, which is not the case if blade speed is used to normalise the thrust and flight speed. This indicates that the aim of decoupling the external aerodynamics from the turbomachinery flow has been achieved using this set of non-dimensional parameters.

The relationship between C_T and ϵ given in Equation (2) is plotted in Fig. 10. The experimentally measured thrust coefficient is below the theoretical prediction across all values of ϵ measured. The difference can be attributed to the residual swirl in the jet and the viscous drag on the nacelle and pylon. The difference between the theoretical and measured C_T increases with ϵ. This is because at low values of ϵ, the jet velocity is large compared to flight speed, meaning the relative magnitude of the external viscous drag forces is small compared to the thrust from the jet momentum change. As ϵ increases, the relative magnitude of the viscous

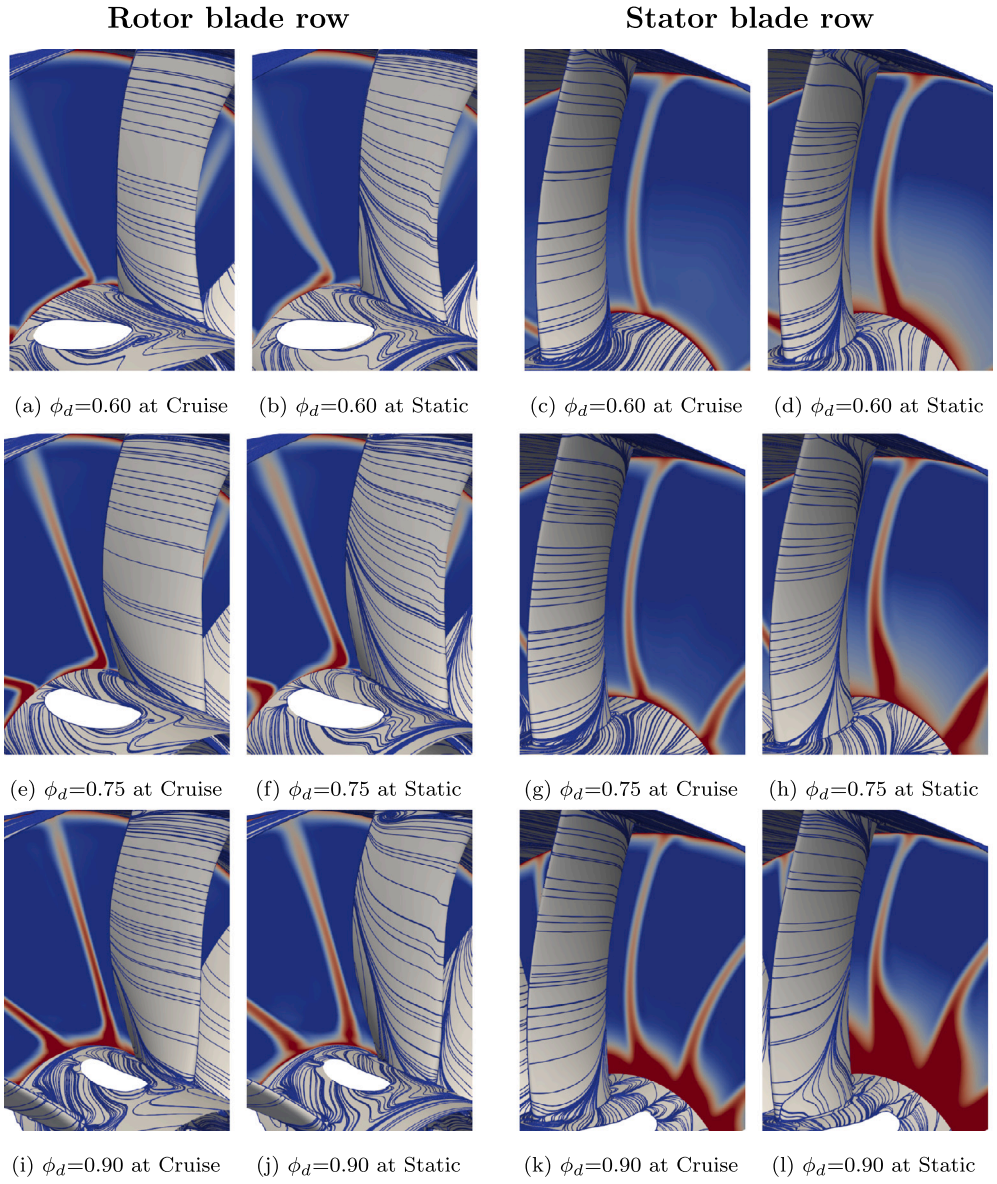

Fig. 15. CFD results of the rotor and stator blades for operation at cruise and static flight conditions showing suction surface streamlines and downstream entropy function contours.

drag forces on the nacelle increase, resulting in an increased difference between the control volume prediction and measured thrust coefficient.

4.2. Intake flowfield

Measurements of static pressure around the intake lip are non-dimensionalised to form a pressure coefficient

$$C_{ps} = \frac{p_s - p_{0,1}}{p_{0,1} - p_1}, \tag{13}$$

where p_s is the static pressure measured at each individual tapping, and p_1 and $p_{0,1}$ are the static and stagnation pressures at the rotor inlet respectively. Fig. 11 shows C_{ps} plotted against non-dimensional axial position X_{ND}, defined as the distance from the intake leading edge to the tapping location divided by the distance from the intake leading edge to the rotor inlet plane. The solid lines are measurements taken on the inside surface of the intake and the dashed lines are measured on the outside.

The shape of the distribution is governed by the value of the jet velocity ratio ϵ. Fig. 11 shows that for $\epsilon = 0.60$, the stagnation point, $C_{ps} = 0$, is located just outside of the intake leading edge at $X_{ND} = 0.01$ and for $\epsilon = 0.94$, the stagnation point lies just on the inside of the intake at $X_{ND} = 0.01$. For both cases, C_{ps} drops on the inside of the duct as the flow accelerates through the intake. The static pressure also drops on the outside of the duct as the flow is accelerated. For $\epsilon = 0.94$, C_{ps} on the outside drops to -1.3 by $X_{ND} = 0.05$ while for $\epsilon = 0.60$, C_{ps} reduces more gradually towards a value of -0.5. This difference is due to the size and shape of the captured streamtube. At low ϵ, upstream captured streamtube area is larger than the intake area, so the flow through the convergent section of the intake is faster than the freestream flow, meaning the external static pressure is higher. At high ϵ, the captured streamtube area upstream is of similar area to the jet, so flow velocity in the converging section of the intake is below freestream velocity, and the static pressure on the outside of the intake is lower than that on the inside.

For the zero flight speed case where $\epsilon = 0$, the stagnation point on the outer surface of the nacelle is located rearward of the outer tapping at $X_{ND} = 0.55$. Flow accelerates from this point on the outside of the duct towards the intake leading edge, measured as a drop in C_{ps} between $X_{ND} = 0.2$ and 0. As the flow passes around the intake leading edge,

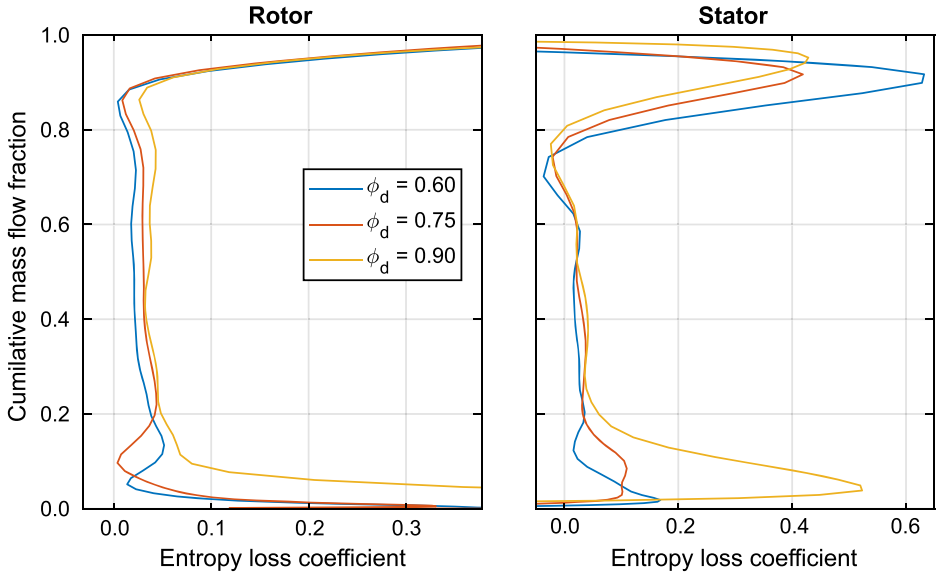

Fig. 16. Blade row loss coefficients calculated from CFD for all three EDF designs at the cruise operating point.

it rapidly decelerates and C_{ps} increases from -1.6 to approximately -1.38 between $X_{ND} = 0$ to 0.02. Between the points A and B, marked in Fig. 11, C_{ps} varies by less than 0.05, indicating the presence of a separation caused by the adverse pressure gradient on the inside of the intake lip. At B, C_{ps} rises gradually from approximately -1.35 to -1 at the rotor inlet, showing that the flow reattaches and decelerates without separation through the rest of the intake. This result is supported by the photograph in Fig. 13, which shows flow visualisation paint "pooling" where the separation bubble is located but flowing backwards after the reattachment line for $\epsilon = 0$. Fig. 13 also shows that for $\epsilon = 0.1$ the intake flow is fully attached, highlighting that the intake separation bubble only occurs at static or very low flight speed conditions.

Fig. 12 shows a meridional view of circumferentially-averaged static and stagnation pressure for the flow passing through the EDF at zero flight speed, $\epsilon = 0$. Static pressure around the nacelle intake shows a suction peak followed by a region of almost constant pressure, similar to the measured results, and flow in the jet is confirmed to be at atmospheric pressure. Stagnation pressure through the intake is uniform except for regions close to the endwalls where thin boundary layers develop.

Overall, the intake measurements show that the aerodynamic design of the duct is balanced. The static condition exhibits a closed separation bubble in the intake, but this can be tolerated, and the conditions measured at $\epsilon = 0.60$ and 0.94 show attached flow on both the inside and outside of the duct.

4.3. Turbomachinery performance

Fig. 14 shows total-to-total pressure rise coefficient, C_{ptt}, and polytropic efficiency, η_{poly}, plotted against flow coefficient, ϕ, for the three different blade designs. Plotted for each case is the ideal pressure rise given by Equation (6), the CFD predicted pressure rise and efficiency, and the experimentally measured pressure rise. The experimental test cases are the same as those plotted in Fig. 10. Unlike the C_T-ϵ, relationship, the different blade designs result in different characteristic lines, with higher design flow coefficient resulting in a larger pressure rise coefficient.

For the pressure rise characteristics, there is good agreement between the CFD simulations and experimental measurements for all three blade designs, the CFD predicts C_{ptt} at design ϕ to within 0.02 of the experimentally measured values.

The CFD simulations reach a lower value of ϕ than the experimental measurements. This is because the left hand point on each experimental characteristic is measured at the static condition, $\epsilon = 0$, and all three blade designs reach this point without stalling. To throttle the fans into stall, the exit duct area would need to be reduced with a variable area nozzle not considered in this study. For the CFD simulations, the exit static pressure boundary condition is varied so that the last stable operating point before the fan stalls is determined.

At the design flow coefficients of 0.60, 0.75 and 0.90, the ideal pressure rise characteristic is above the CFD and experimental characteristics because it does not include aerodynamic loss which is modelled by CFD and measured in the experiment. To the left of the design points, the ideal pressure rise characteristics diverge further because Equation (6) also assumes constant deviation angle. In reality deviation angle increases as flow coefficient reduces. This means that flow turning through the blade row is reduced in comparison to the ideal case. This mechanism, alongside the increasing loss, causes the simulated and experimental characteristics to "roll over" when compared to the ideal line.

To the right of the design flow coefficients, the loss increases as the blade experiences negative incidence. However, negative incidence reduces deviation and the assumption of constant deviation angle for the ideal characteristic underpredicts flow turning. This explains why the measured pressure rise for the $\phi_d = 0.60$ and $\phi_d = 0.75$ designs exceed the ideal characteristic at flow coefficients above 0.68 and 0.90 respectively. For the $\phi_d = 0.90$ design, the balance between increased loss and reduced deviation means that the ideal line is above the simulated and measured data across the measured operating range.

The three different designs have different efficiency characteristics. The $\phi_d = 0.75$ design has the highest efficiency as well as the widest peak, operating above 76% for $0.52 < \phi < 0.72$. In all three designs the peak efficiency is observed to occur at a flow coefficient less than their design flow coefficients ϕ_d. This is expected for these designs which have a conservative maximum diffusion factor at the design point of 0.4. Fig. 5 shows that across most of their span, the blades have margin to deliver higher loading with low loss as the EDF is throttled.

4.4. Turbomachinery flow structures

In this section an analysis of the loss sources in the different designs is used to understand why the $\phi_d = 0.75$ design has the highest aerodynamic performance. Fig. 15 shows contours of entropy function, an indicator of loss generation independent of blade frame of reference, downstream of the rotor and stator rows for each of the three designs at

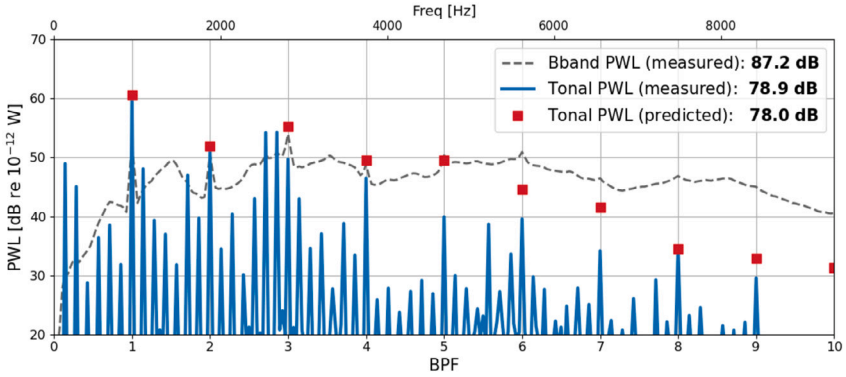

(a) $\phi_d = 0.60$

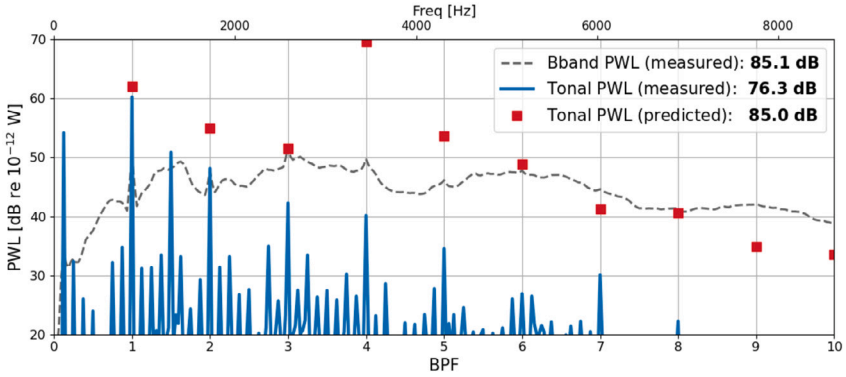

(b) $\phi_d = 0.75$

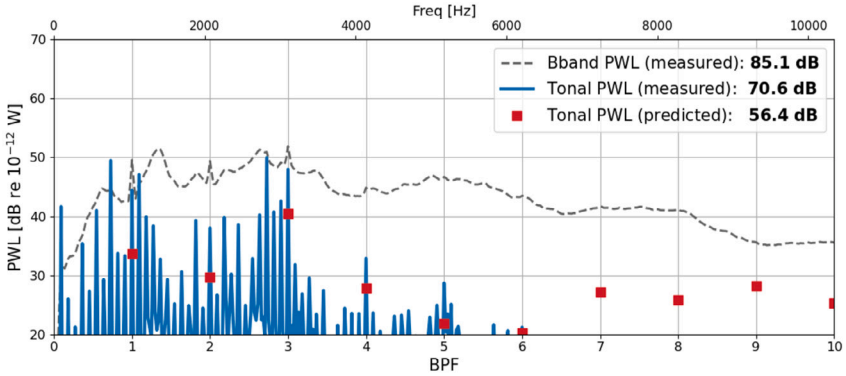

(c) $\phi_d = 0.90$

Fig. 17. Comparison between Sound Power Level (PWL) spectra for the experimental data broken down into broadband and tonal components and the tonal numerical acoustic predictions.

cruise and static flight conditions. Plotted on the suction surface of each blade are surface limiting streamlines which can be used to identify the types of flow structure present in each region as in [30].

In all cases and at all operating points, the flow on the rotor is attached. At static conditions, and especially for the $\phi_d = 0.90$ design, there are corner separations at the hub end but they remain closed and well behaved. However, at the hub end of the stators for the $\phi_d = 0.90$ design the corner separations are open at the static condition, causing significant loss in performance which can be seen in the efficiency characteristic in Fig. 14. The other two flow coefficients instead show trailing edge separations across the entire span, and are therefore more balanced designs. As a general design guideline, the operating range of high flow coefficient designs can be improved by including more 3D geometry, such as sweep or lean, than is required for low or moderate flow coefficient designs.

At the cruise operating point the balance between endwall and profile loss sources depends on the design flow coefficient. For $\phi_d = 0.90$ the loss shown in the wake is increased, the wakes become deeper as diffusion is increased for these more highly loaded designs, this loss source is multiplied by the required increase in the number of blades. Fig. 16 plots circumferentially-averaged entropy loss coefficient against cumulative mass flow fraction[7] across the blade span. This shows quan-

[7] For example, at a spanwise position with cumulative mass flow fraction 0.4, 40% of mass flow is below and 60% above.

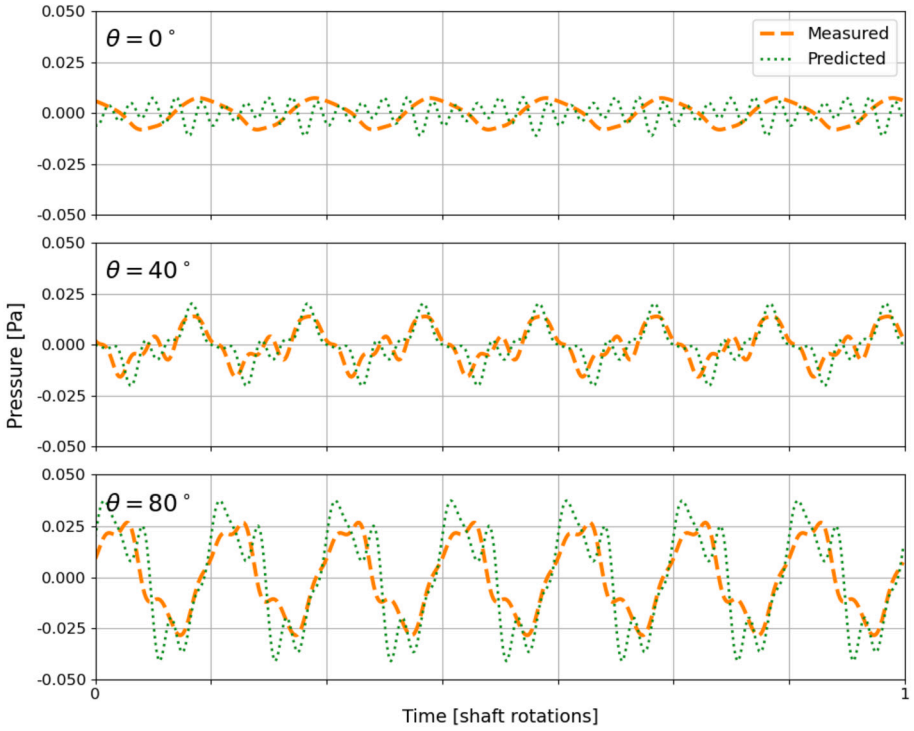

Fig. 18. Comparison between measured and predicted acoustic pressures for $\phi_d = 0.60$ blade design at three emission angles, all signals are synthesized from the first 5 BPF harmonics only.

titatively the increase in loss for the $\phi_d = 0.90$ design in the 20-80% mass flow fraction region on both rotor and stator rows.

Endwall losses are greater at both ends of the design space represented by the $\phi_d = 0.60$ and $\phi_d = 0.90$ designs, although it occurs in different locations. For the $\phi_d = 0.60$ design the loss is increased on the endwall surfaces, at the casing end of the rotor the shroud ring has a higher relative velocity. This swirls up the flow and increases losses seen between 80-100% mass flow fraction in the stator row. For the $\phi_d = 0.90$ design the issue is in the hub sections of the stage with larger corner separations, therefore increased losses are seen between 0-20% mass flow fraction in both blade rows. Combining these effects together means that overall efficiency is maximised for the most balanced $\phi_d = 0.75$ design as seen in the overall efficiency characteristics of Fig. 14.

5. Acoustic performance

This section describes the aeroacoustic measurements performed at static conditions, $\epsilon = 0$, in the University of Salford Anechoic Chamber using the EDF with different blade sets, and compares the measured tonal noise data to the simulated tonal noise predictions.

5.1. Sound power level spectra and tonal reconstruction

Fig. 17 shows the Sound Power Level (PWL) spectra for all designs. The dashed grey line shows the measured broadband noise PWL, i.e. the residual component, which dominates the sound radiation and presents similar levels for all three blade designs. The solid blue lines show the measured tonal noise PWL, i.e. the rotor-locked component, exhibiting multiple tones at both shaft frequency harmonics and BPF harmonics, and the red squares show the predicted tonal noise PWL obtained from the acoustic numerical predictions at the BPF harmonics. The integrated PWL is indicated in the Figure legend. A good agreement is observed for the first few BPF harmonics for the $\phi_d = 0.60$ and $\phi_d = 0.75$ blade designs, whereas at higher harmonics the tonal noise is overpredicted. This results in an overall good prediction capability of the tonal noise PWL for the $\phi_d = 0.60$ design, although the $\phi_d = 0.75$ design is overpredicted at the higher harmonics, and the $\phi_d = 0.90$ design is underpredicted at all dominant harmonics.

Due to inaccuracies in manufacture, such as slight asymmetries between the blades in each row, and in the measurement setup, for example the imperfect rotor balancing, the measured signals exhibit significant energy at shaft frequency harmonics as well as blade-passing harmonics. To allow a proper comparison between predictions and measurements, the complex amplitudes of the first five BPF harmonics are extracted from both predictions and measurements using a Fourier Transform, and the time-domain signals re-synthesized to remove the influence of shaft frequency tones for the measurements and higher-order harmonics for both the predictions and measurements.

Fig. 18 compares the measured and predicted acoustic pressures of the first five BPF harmonics for the $\phi_d = 0.60$ blade design at emission angles $\theta = [0°, 40°, 80°]$. A good agreement is obtained at $\theta = 40°$ and $\theta = 80°$ with the predicted acoustic waveforms matching the measured waveforms in both amplitude and phase, although some disagreement is observed in the waveform details at high frequencies. There is a larger disagreement at $\theta = 0°$, where the predicted signal does not capture the fundamental BPF tone correctly and instead shows more energy in the higher BPF harmonics.

5.2. Acoustic directivity

Fig. 19 compares the measured and predicted directivity of the first five BPF harmonics and of the broadband noise for all blade designs. The measured broadband noise levels are shown as a light grey dashed line, the measured tonal noise levels are shown as a dash-dotted orange line, and the predicted tonal noise levels are shown as a dotted green line. Despite the difference in rotational speeds, the measured broadband noise directivities are broadly similar between the different designs, while the tonal noise levels reduce significantly with increasing flow coefficient ϕ_d.

For the $\phi_d = 0.60$ blade design shown in Fig. 19a, the predicted tonal noise directivity agrees well with the measured directivity. The small "notch" observed in the measured data at $\theta = 60°$ is not as pronounced

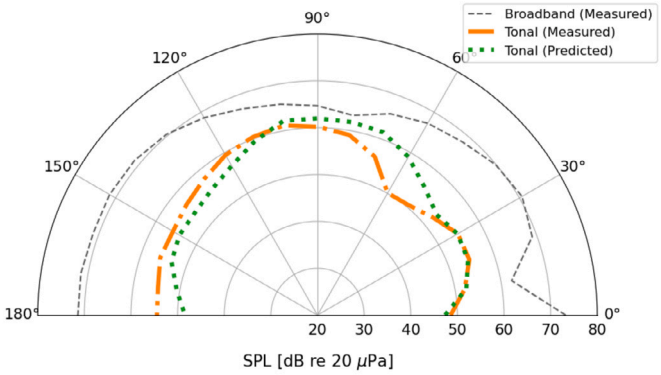

(a) $\phi_d = 0.60$

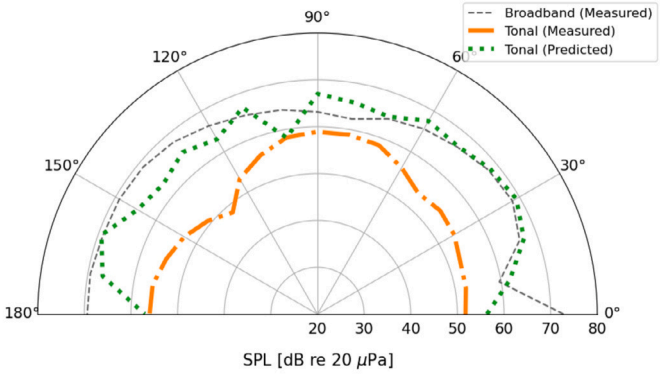

(b) $\phi_d = 0.75$

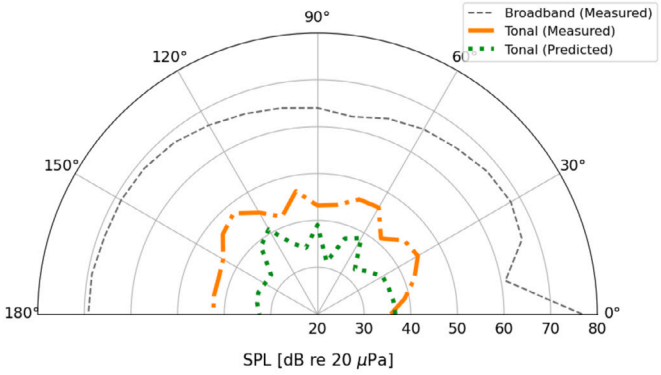

(c) $\phi_d = 0.90$

Fig. 19. Comparison between measured and predicted acoustic directivity for different blade designs, all tonal signal levels are extracted from the first 5 BPF harmonics.

in the predicted data, and appears instead at $\theta = 40°$. For the $\phi_d = 0.75$ design in Fig. 19b, the tonal noise levels are overpredicted in almost all directions, whereas for the $\phi_d = 0.90$ design in Fig. 19c, the levels are underpredicted in all directions. However, looking at all three designs together, the relative trends in tonal SPL are captured well by the predictions, and this would drive a designer towards the high flow coefficient blades with their reduced tonal noise.

6. Psychoacoustics and multi-disciplinary design

The design flow coefficient of an EDF has been shown to affect the aerodynamic and acoustic performance of the machine. An optimum design exists for aerodynamic efficiency whereas tonal sound power levels are reduced when the flow coefficient is increased as much as possible. This section introduces further metrics and how they can be traded against each other. Beginning with the psychoacoustic performance, these metrics capture how the noise is actually perceived by an observer and how annoying they might find the sound from the different EDF designs. This section ends by considering the impact that the design flow coefficient can have on the choice of electric machine and its affect on the structural performance of the rotor.

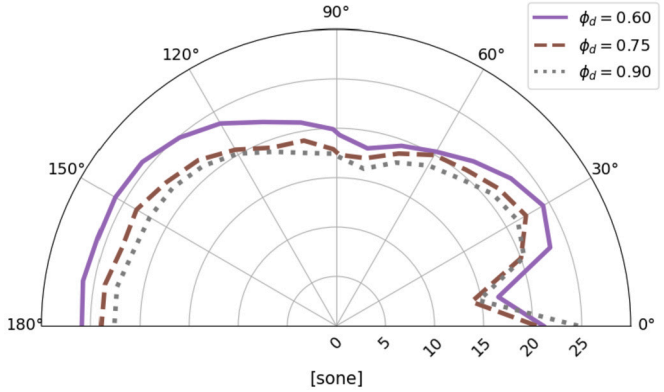

Fig. 20. Loudness (DIN 45631/A1 model) for three EDF designs.

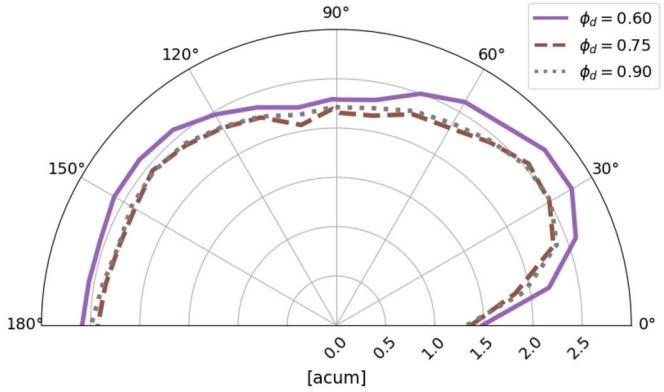

Fig. 21. Sharpness (DIN 45692 model) for three EDF designs.

6.1. Psychoacoustic analysis

The noise recordings from the EDF are exported as .WAV files and processed through HEAD Acoustic ArtemiS Suite 12.0 software to calculate a series of Sound Quality Metrics (SQMs). All time series are processed to remove the first 0.5 s to avoid transient effects in the calculations. The 5^{th} percentiles, or 5% exceedance levels [41], are also calculated to represent the higher range of each SQM time history.

Figs. 20, 21 and 22 show the values of Loudness (DIN 45631/A1 model), Sharpness (DIN 45692 model) and Tonality (Sottek's Hearing Model [42]) for all emission angles and each blade design. A decrease in Loudness is observed with an increase in design flow coefficient in Fig. 20. Similar results are observed by Klähn et al. [43], where it was found that the rotor-stator interaction broadband noise decreased with increasing flow rate. Sharpness, which represents the perceived high frequency content, also decreases with an increase in flow coefficient in Fig. 21, although the designs with $\phi_d = 0.75$ and 0.90 have a similar relative content of high frequency. The larger corner separations observed at the stator blades at static conditions for $\phi_d = 0.90$ in Fig. 15, causes increased turbulence-trailing edge interaction noise and leads to an increase in high-frequency broadband noise radiation relative to lower design flow coefficients, even if the tonal noise from the blade passing is reduced.

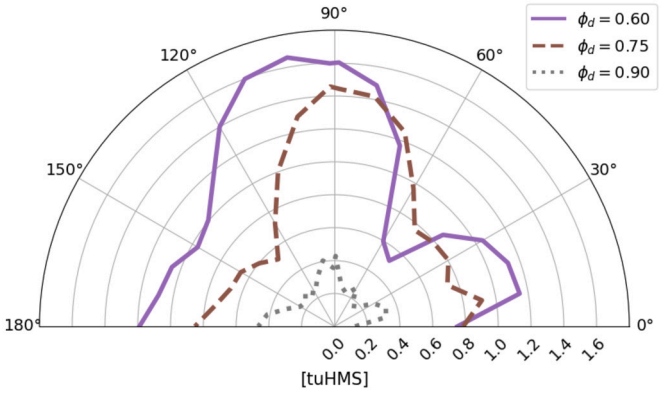

Fig. 22. Tonality (Sottek's Hearing Model) for three EDF designs.

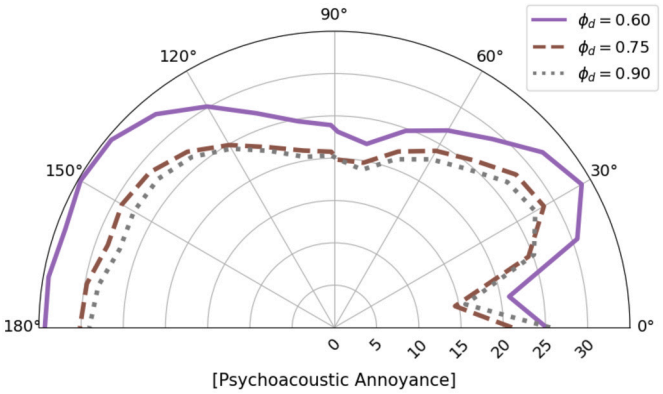

Fig. 23. Zwicker's Psychoacoustic Annoyance for three EDF designs.

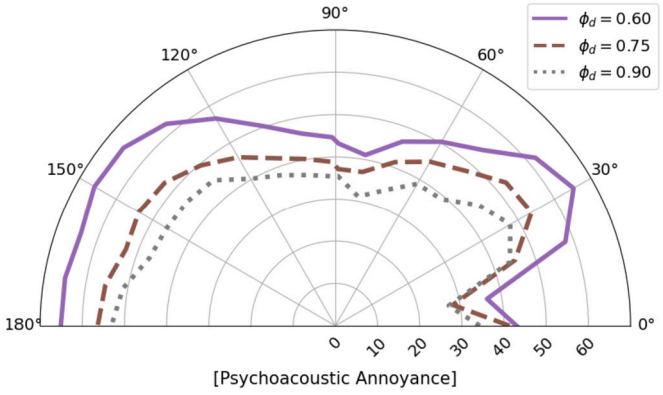

Fig. 24. More's Psychoacoustic Annoyance for three EDF designs.

The largest difference between the blade designs is the Tonality metric. As shown in Fig. 22, a steep reduction in Tonality is observed with increasing design flow coefficient. The designs with $\phi_d = 0.60$, 0.75 and 0.90 have 7, 8 and 11 rotor blades respectively. These combined with the rotational frequencies shown in Table 1 give blade passing frequencies of 936 Hz, 862 Hz and 1034 Hz, respectively. The reduction in tonal noise is possibly due to the decrease in radiation efficiency as the number of rotor and stator blades increases. This phenomenon has been discussed in the literature for open propellers [44]. Further research is required to confirm this hypothesis also applies to a ducted fan design.

As discussed by Torija et al. [45], the perception of sounds generated by aerodynamic phenomena is a complex process due to the number of psycho-acoustic features involved including tonal noise, high frequency noise and time varying noise. For this reason, several so-called Psychoacoustic Annoyance (PA) models integrating the psychoacoustic metrics have been developed. The most widely used is the model developed by Zwicker and Fastl [46], where relative annoyance degrees for a given noise are estimated from measures of Loudness, Sharpness, Fluctuation Strength and Roughness, the latter two account for slow and rapid amplitude modulation of the sound level. Based on the results of seven psychoacoustic tests for aircraft noise samples with varying metrics, More [47] developed a modified version of Zwicker and Fastl's PA model. The two main differences between these PA models are that More's model includes a calculation of Tonality, and is optimised for aircraft noise annoyance. When plotting the values of PA calculated with Zwicker's model in Fig. 23, both designs with $\phi_d = 0.75$ and 0.90 show similar values of PA, and are lower than the $\phi_d = 0.60$ by five points across all emission angles. However, when Tonality is considered in the calculation of PA using More's model, Fig. 24) shows a continual decrease in PA as design flow coefficient is increased.

6.2. Electric motor matching

The overall system efficiency is the combination of aerodynamic and electrical efficiency. Increasing the design flow coefficient requires an increase in the torque requirement at the expense of rotation speed. For a given motor the power losses are a sum of the different components [48]

$$P_{loss} = k_c I^2 + k_i \omega + k_w \omega^3 + C, \tag{14}$$

where k_c, k_i, k_w and C are copper, iron, windage and constant loss coefficients respectively. In this study, the balance of these loss sources will be shifted with different EDF designs with varying flow coefficient. The $\phi_d = 0.60$ design runs at the highest speed and lowest torque and, focusing on just the most significant two sources, therefore has a higher iron loss and lower copper loss. On the other hand, the $\phi_d = 0.90$ design requires 42% higher torque and therefore the copper loss dominates. In order to address this, it is likely that a motor matched to drive an EDF with $\phi_d = 0.90$, would have to be heavier with thicker windings to try and reduce resistive power dissipation.

6.3. Mechanical constraints

Weight is of primary importance for aerospace applications and therefore many components in the EDF are stressed close to the yield limits of their respective materials. The most critical components are the rotating structures and in these designs the two most highly stressed locations are the blade roots at the hub end and the circumferential shroud ring that joins the rotor tips together. For either of these locations it can be shown that

$$\sigma_{rotor} \propto \rho_{rotor}\, \omega^2. \tag{15}$$

The $\phi_d = 0.90$ design rotates at 70% of the rotational speed of the $\phi_d = 0.60$ design and therefore experiences 49% of the stress. This could benefit the design of the EDF either by reducing the required material thicknesses, improving aerodynamic efficiency and saving weight, or by allowing an increase in rotational speed to achieved higher thrust or faster flight speeds within the same diameter engine. (See Fig. 25.)

6.4. Design guidelines

Using a combination of experimental and numerical methods this paper has shown that the design with $\phi_d = 0.75$ is optimum for aerodynamic efficiency, it also has the widest region of high efficiency and draws the least power during take-off. It has also demonstrated that the $\phi_d = 0.90$ design has the least psychoacoustic annoyance and as such would be perceived as the best design for operating close to the public in busy urban environments. However, designers also need to consider the electrical and mechanical design of these machines as although the $\phi_d = 0.90$ EDF design has the lowest stress, it is also likely to require the

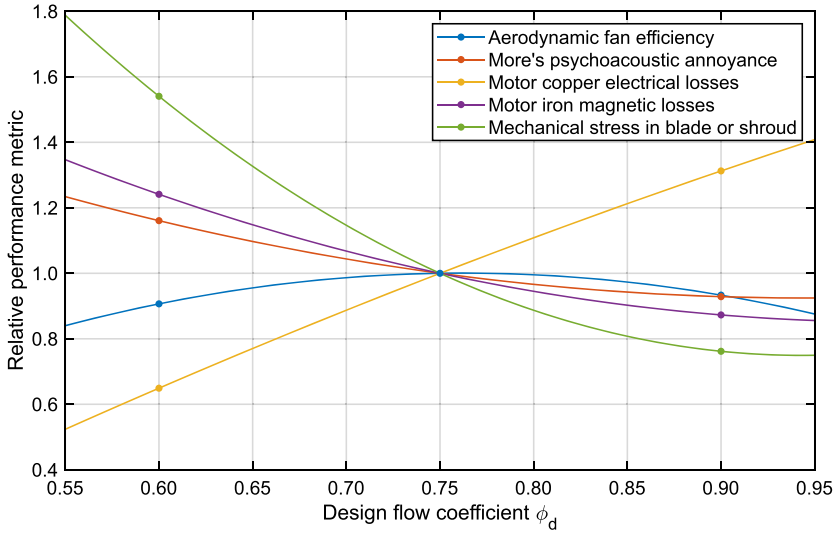

Fig. 25. Multi-disciplinary performance tradeoffs in selecting design flow coefficient.

Fig. 26. Integrated propulsion module (IPM) developed for flight testing [Courtesy of Greenjets Ltd.]

heaviest electric motor to turn the rotor at its relatively higher torque. The results of this paper were used to inform the design of a specific EDF shown in Fig. 26 for a civilian surveillance application where all of these multi-disciplinary constraints are active.

7. Conclusions

A methodology is presented for the design of electric ducted fans and the subsequent exploration of the design space. With inverse aerodynamic design it is possible to create families of designs where only a single design parameter is varied to understand its effect. In this paper the design flow coefficient is changed and three blade designs with values of $\phi_d = 0.60, 0.75$ and 0.90 created. The design flow coefficient is shown to have a first-order effect on the aerodynamic performance and psychoacoustic annoyance, as well as the electrical and mechanical performance, and should therefore be considered as a multidisciplinary design variable.

Increasing flow coefficient achieves the same thrust level at reduced shaft speed, however the stage loading coefficient at a given operating point rises and increased blade counts are therefore required. A design with optimum aerodynamic efficiency was found at $\phi_d = 0.75$. While all designs had adequate operating range to operate at static conditions without stall, the $\phi_d = 0.75$ design also had the most operating range in reserve.

A hybrid acoustic prediction scheme is adopted, allowing the use of a well-established CFD solver including complex geometric and flow features, together with a computationally efficient acoustic solver to predict the far-field tonal noise. Special processing methods are required to compare the idealised acoustic predictions with the imperfect acoustic measurements. The tonal noise radiation predictions are partially successful: while a good agreement between predictions and measurements is observed for the lowest flow coefficient, other blade designs show either over- or underprediction issues, indicating a need for further research.

The noise radiation from all blade designs is dominated by broadband noise, which does not change significantly in overall level and directivity between the iterations at constant thrust. It is hypothesised that the flow separation features observed at static conditions at the intake and at the stator blades' trailing edge generated increased turbulence-interaction noise at the rotor and stator, respectively. As no flow separation is expected when operating the EDF in flight conditions, the broadband noise levels in flight should be lower than the levels observed in static conditions. Sound radiation changes when operating propellers under static and flight conditions are well known in the literature [49,23], but the present analysis can help identify the physical mechanisms behind such behaviour in ducted fans and point to future noise reduction approaches. Although acoustic measurements at static conditions are representative of take-off situations and are therefore relevant for assessing aircraft noise impacts on the general public, further acoustic testing of the EDF in flight conditions is required to fully understand its noise performance.

Increasing design flow coefficient from 0.60 to 0.90 reduces tonal noise radiated by the EDF by a factor of three. This is possibly due to the increase in number of rotor and stator blades resulting in the excitation of higher-order acoustic modes, which have reduced acoustic radiation efficiency. This mechanism of tonal noise reduction has been described for isolated propellers [44], but could also help explain the EDF performance due to the short duct length compared to the acoustic wavelengths. The reduction in tonal noise results in significant improvements to Sound Quality Metrics, with Tonality and More's Psychoacoustic Annoyance in particular exhibiting the largest changes with design flow coefficient. The best acoustic results were obtained for the $\phi_d = 0.90$ blade design. The optimal balance between aerodynamic and acoustic metrics is likely to be in the range $\phi_d = 0.75$ and $\phi_d = 0.90$.

Psychoacoustic performance is the most important metric in determining public acceptance of large numbers of electric vehicles operating in the near future. It is recommended that designers and operators aim to push design flow coefficients as high as possible without excessively

compromising the aerodynamic efficiency in order to reduce the impact of their machines on the world.

Funding sources

The Authors would like to acknowledge the funding provided by Innovate UK for the InCEPTion project (ref. 73692). Antonio J. Torija would like to also acknowledge the funding provided by the UK Engineering and Physical Sciences Research Council for the DroneNoise project (EP/V031848/1).

CRediT authorship contribution statement

Fabio Casagrande Hirono: Writing – original draft, Visualization, Software, Investigation, Formal analysis, Conceptualization. **Antonio J. Torija:** Writing – original draft, Visualization, Project administration, Investigation, Funding acquisition, Formal analysis, Conceptualization. **Sam D. Grimshaw:** Writing – original draft, Visualization, Software, Investigation, Formal analysis, Conceptualization. **Dominic Cousins:** Writing – original draft, Visualization, Software, Investigation, Formal analysis, Conceptualization. **Judith Farman:** Writing – original draft, Visualization, Software, Investigation, Formal analysis, Conceptualization. **James V. Taylor:** Writing – original draft, Visualization, Software, Investigation, Funding acquisition, Formal analysis, Conceptualization.

Declaration of competing interest

The authors declare the following financial interests/personal relationships which may be considered as potential competing interests: Fabio Casagrande Hirono, Antonio J. Torija, Sam D. Grimshaw, Dominic Cousins, Judith Farman, James V. Taylor reports financial support was provided by Innovate UK. Antonio J. Torija reports financial support was provided by Engineering and Physical Sciences Research Council. If there are other authors, they declare that they have no known competing financial interests or personal relationships that could have appeared to influence the work reported in this paper.

Data availability

Data will be made available on request.

Acknowledgements

The Authors would like to acknowledge Dr Andrew Elliott and Dr Carlos Ramos Romero of the University of Salford, and Dr Demetrios Lefas of the University of Cambridge for their assistance in designing and conducting the experiments described herein. We would also like to thank Prof Kenneth Brentner and Dr Eric Greenwood, from Penn State University, USA, for providing access to their aeroacoustic prediction software PSU-WOPWOP. We would also like to thank Greenjets Ltd.[8] for their permission to use the photograph in Fig. 26 and for supporting this research project.

References

[1] D.P. Thipphavong, R. Apaza, B. Barmore, V. Battiste, B. Burian, Q. Dao, M. Feary, S. Go, K.H. Goodrich, J. Homola, H.R. Idris, P.H. Kopardekar, J.B. Lachter, N.A. Neogi, H.K. Ng, R.M. Oseguera-Lohr, M.D. Patterson, S.A. Verma, Urban air mobility airspace integration concepts and considerations, in: 2018 Aviation Technology, Integration, and Operations Conference, American Institute of Aeronautics and Astronautics, 2018.

[2] R. Whittle, Air mobility bonanza beckons electric VTOL developers, vertiflite magazine, https://vtol.org/files/dmfile/Whittle-Electric-VTOL-MA171.pdf, 2017.

[3] P. Nathen, A. Bardenhagen, A. Strohmayer, R. Miller, S. Grimshaw, J. Taylor, Architectural performance assessment of an electric vertical take-off and landing (e-vtol) aircraft based on a ducted vectored thrust concept, Online, 2021. URL: https://lilium.com/files/redaktion/refresh_feb2021/investors/Lilium_7-Seater_Paper.pdf.

[4] F. Casagrande Hirono, A. Torija Martinez, A. Elliott, J. Taylor, S. Grimshaw, D. Lefas, Aeroacoustic design and optimisation of an all-electric ducted fan propulsion module for low-noise impact, in: 28th AIAA/CEAS Aeroacoustics 2022 Conference, American Institute of Aeronautics and Astronautics, 2022.

[5] E. Benini, C. Mistry, A.R. Wadia, Historical developments in fan technologies for aeroengines, in: Volume 13A: Turbomachinery — Axial Flow Fan and Compressor Aerodynamics, American Society of Mechanical Engineers, 2023, https://asmedigitalcollection.asme.org/GT/proceedings-abstract/GT2023/87080/V13AT29A013/1168468.

[6] T. Zhang, G. Barakos, Review on ducted fans for compound rotorcraft, Aeronaut. J. 124 (2020) 941–974, https://doi.org/10.1017/aer.2019.164, https://www.cambridge.org/core/product/identifier/S0001924019001647/type/journal_article.

[7] A. Bacchini, E. Cestino, Electric VTOL configurations comparison, Aerospace 6 (2019) 26, https://doi.org/10.3390/aerospace6030026, https://www.mdpi.com/2226-4310/6/3/26.

[8] D. Weintraub, J. Koppelberg, J. Köhler, P. Jeschke, Ducted fans for hybrid electric propulsion of small aircraft, CEAS Aeronaut. J. 13 (2022) 471–485, https://doi.org/10.1007/s13272-022-00573-7, https://link.springer.com/article/10.1007/s13272-022-00573-7.

[9] R.D. Hine, J.R. Farman, S.D. Grimshaw, J.V. Taylor, Short ducted fan diffusers with integral splitter blades, in: Volume 13C: Turbomachinery - Deposition, Erosion, Fouling, and Icing; Design Methods and CFD Modeling for Turbomachinery; Ducts, Noise, and Component Interactions, American Society of Mechanical Engineers, 2023, https://asmedigitalcollection.asme.org/GT/proceedings-abstract/GT2023/87103/V13CT33A005/1168577.

[10] D. Jedamski, V. Ahuja, E.J. Alvarez, V.K. Lakshminarayan, M. Moore, Distributed electric propulsion and vehicle integration with ducted fans, in: AIAA AVIATION 2023 Forum, American Institute of Aeronautics and Astronautics, 2023, https://arc.aiaa.org/doi/abs/10.2514/6.2023-3455.

[11] M. Moore, X. Fei, D. Jedamski, A. Perry, L.A.M. Ramirez, I. Villa, V.K. Lakshminarayan, Unlocking low-cost regional air mobility through whisper aero-propulsive coupling, in: AIAA AVIATION 2023 Forum, American Institute of Aeronautics and Astronautics, 2023, https://arc.aiaa.org/doi/abs/10.2514/6.2023-3456.

[12] F. Farassat, Derivation of Formulations 1 and 1A of Farassat, NASA Technical Memorandum NASA/TM-2007-214853 NASA Langley Research Center, Hampton, VA, United States, 2007, https://ntrs.nasa.gov/citations/20070010579.

[13] J.E. Ffwocs Williams, D.L. Hawkings, Sound generation by turbulence and surfaces in arbitrary motion, Philos. Trans. R. Soc. Lond. Ser. A, Math. Phys. Sci. 264 (1969) 321–342, https://doi.org/10.1098/rsta.1969.0031, https://royalsocietypublishing.org/doi/10.1098/rsta.1969.0031.

[14] S. Moreau, Turbomachinery noise predictions: present and future, Acoustics 1 (2019) 92–116, https://doi.org/10.3390/acoustics1010008.

[15] S. Moreau, A review of turbomachinery noise: from analytical models to high-fidelity simulations, in: Notes on Numerical Fluid Mechanics and Multidisciplinary Design, Springer International Publishing, 2020, pp. 579–595.

[16] T. Jardin, R. Gojon, N. Doué, H. Parisot-Dupuis, Numerical and experimental analysis of the influence of solidity on rotor aeroacoustics at low Reynolds numbers, Int. J. Aeroacoust. (2023), 1475472X2211501, https://doi.org/10.1177/1475472x221150181.

[17] D. Weitsman, E. Greenwood, Parametric study of eVTOL rotor acoustic design trades, in: AIAA Scitech 2021 Forum, American Institute of Aeronautics and Astronautics, 2021, https://arc.aiaa.org/doi/10.2514/6.2021-1987.

[18] G. Brès, K. Brentner, G. Perez, H. Jones, Maneuvering rotorcraft noise prediction, J. Sound Vib. 275 (2004) 719–738, https://doi.org/10.1016/j.jsv.2003.07.005, https://linkinghub.elsevier.com/retrieve/pii/S0022460X03008630.

[19] K.S. Brentner, F. Farassat, Modeling aerodynamically generated sound of helicopter rotors, Prog. Aerosp. Sci. 39 (2003) 83–120, https://doi.org/10.1016/S0376-0421(02)00068-4, https://linkinghub.elsevier.com/retrieve/pii/S0376042102000684.

[20] P.R. Spalart, K.V. Belyaev, M.L. Shur, M. Kh Strelets, A.K. Travin, On the differences in noise predictions based on solid and permeable surface Ffowcs Williams–Hawkings integral solutions, Int. J. Aeroacoust. 18 (2019) 621–646, https://doi.org/10.1177/1475472X19878934, http://journals.sagepub.com/doi/10.1177/1475472X19878934.

[21] A.F. Ribeiro, M.R. Khorrami, R. Ferris, B. Koenig, P.A. Ravetta, Lessons learned on the use of data surfaces for ffowcs Williams-Hawkings calculations: airframe noise applications, in: 28th AIAA/CEAS Aeroacoustics 2022 Conference, American Institute of Aeronautics and Astronautics, 2022.

[22] S. Moreau, Y. Pasco, G. Yakhina, Aeroacoustic investigation of an urban-air-mobility ducted fan, in: 28th AIAA/CEAS Aeroacoustics 2022 Conference, American Institute of Aeronautics and Astronautics, 2022.

[23] A.M. Malgoezar, A. Vieira, M. Snellen, D.G. Simons, L.L. Veldhuis, Experimental characterization of noise radiation from a ducted propeller of an

[8] URL. https://www.greenjets.com/.

unmanned aerial vehicle, Int. J. Aeroacoust. 18 (2019) 372–391, https://doi.org/10.1177/1475472X19852952, http://journals.sagepub.com/doi/10.1177/1475472X19852952.
[24] D.R. Cuppoletti, T. Riley, Time-resolved flow field and acoustic measurements of a ducted and unducted rotor, in: 28th AIAA/CEAS Aeroacoustics 2022 Conference, American Institute of Aeronautics and Astronautics, 2022.
[25] F. Simon, N.H. Schiller, N.S. Zawodny, N.A. Pettingill, M.B. Galles, Fundamental noise characterization of a ducted propeller in hover, in: INTER-NOISE and NOISE-CON Congress and Conference Proceedings, vol. 265, 2023, pp. 657–667.
[26] S.L. Dixon, C.A. Hall, Fluid Mechanics and Thermodynamics of Turbomachinery, Elsevier, 2010, https://linkinghub.elsevier.com/retrieve/pii/C20090202054.
[27] S. Lieblein, F.C. Schwenk, R.L. Broderick, Diffusion Factor for Estimating Losses and Limiting Blade Loadings in Axial-Flow-Compressor Blade Elements, NACA Research Memorandum NACA-RM-E53D01, National Advisory Committee for Aeronautics (NACA), 1953, https://digital.library.unt.edu/ark:/67531/metadc59727/.
[28] A.R. Howell, Design of axial compressors, Proc. Inst. Mech. Eng. 153 (1945) 452–462, https://doi.org/10.1243/PIME_PROC_1945_153_050_02, http://journals.sagepub.com/doi/10.1243/PIME_PROC_1945_153_050_02.
[29] B.M. Kulfan, Universal parametric geometry representation method, J. Aircr. 45 (2008) 142–158, https://doi.org/10.2514/1.29958, https://arc.aiaa.org/doi/10.2514/1.29958.
[30] J.V. Taylor, R.J. Miller, Competing three-dimensional mechanisms in compressor flows, J. Turbomach. 139 (2017) 021009, https://doi.org/10.1115/1.4034685, https://asmedigitalcollection.asme.org/turbomachinery/article/doi/10.1115/1.4034685/378819/Competing-ThreeDimensional-Mechanisms-in.
[31] P. Spalart, S. Allmaras, A one-equation turbulence model for aerodynamic flows, in: 30th Aerospace Sciences Meeting and Exhibit, American Institute of Aeronautics and Astronautics, Reno, NV, U.S.A., 1992, https://arc.aiaa.org/doi/10.2514/6.1992-439.
[32] T. Brandvik, G. Pullan, An accelerated 3d Navier–Stokes solver for flows in turbomachines, J. Turbomach. 133 (2010), https://doi.org/10.1115/1.4001192.
[33] A. Jameson, Time dependent calculations using multigrid, with applications to unsteady flows past airfoils and wings, in: 10th Computational Fluid Dynamics Conference, American Institute of Aeronautics and Astronautics, 1991.
[34] S.D. Grimshaw, J.V. Taylor, Fast settling millimetre-scale five-hole probes, in: Volume 6: Ceramics; Controls, Diagnostics and Instrumentation, Education; Manufacturing Materials and Metallurgy, GT2016, American Society of Mechanical Engineers, 2016.
[35] M.J. Dunkley, The aerodynamics of intermediate pressure turbines, Ph.D. thesis, 1998, https://doi.org/10.17863/CAM.19055.
[36] F. Casagrande Hirono, A. Torija Martinez, A. Elliott, Optimization of a contra-rotating propeller rig for reduced psychoacoustic impact, in: Proceedings of Internoise, 2022.
[37] J. Antoni, Cyclostationarity by examples, Mech. Syst. Signal Process. 23 (2009) 987–1036, https://doi.org/10.1016/j.ymssp.2008.10.010, https://linkinghub.elsevier.com/retrieve/pii/S0888327008002690.
[38] L. Grizewski, M. Behn, S. Funke, H.A. Siller, Cyclostationary analysis of fan noise influenced by an inflow control device, AIAA J. 59 (2021) 2578–2589, https://doi.org/10.2514/1.j059493.
[39] A. Pereira, M.C. Jacob, Modal analysis of in-duct fan broadband noise via an iterative Bayesian inverse approach, J. Sound Vib. 520 (2022) 116633, https://doi.org/10.1016/j.jsv.2021.116633, https://www.sciencedirect.com/science/article/pii/S0022460X21006416.
[40] L. Caldas, R. Meyer, New method to separate turbulence statistics of fan rotor wakes from background flow, Exp. Fluids 64 (2023), https://doi.org/10.1007/s00348-023-03576-0.
[41] S. Krishnamurthy, A. Christian, S.A. Rizzi, Psychoacoustic test to determine sound quality metric indicators of rotorcraft noise annoyance, in: INTER-NOISE and NOISE-CON Congress and Conference Proceedings, Chicago, IL, 2018, p. 12, https://www.ingentaconnect.com/content/ince/inceep/2018/00000258/00000007/art00032.
[42] J. Becker, R. Sottek, T. Lobato, Progress in tonality calculation, in: Proceedings of the 23rd International Congress on Acoustics, RWTH Aachen University, Aachen, Germany, 2019, http://publications.rwth-aachen.de/record/769652.
[43] L. Klähn, A. Moreau, L. Caldas, U. Tapken, Assessment of in-duct fan broadband noise measurements in a modern low-speed test rig, in: International Conference of Fan Noise, Aerodynamics, Applications and Systems 2022, Senlis, France, 2022, https://elib.dlr.de/193955/.
[44] D.C. Akiwate, P. Joseph, A. Parry, C. Paruchuri, On the balance between the tonal and broadband noise of isolated propellers, Int. J. Aeroacoust. (2024), https://doi.org/10.1177/1475472X231225631.
[45] A.J. Torija, P. Chaitanya, Z. Li, Psychoacoustic analysis of contra-rotating propeller noise for unmanned aerial vehicles, J. Acoust. Soc. Am. 149 (2021) 835–846, https://doi.org/10.1121/10.0003432, https://asa.scitation.org/doi/10.1121/10.0003432.
[46] H. Fastl, E. Zwicker, Psychoacoustics, 3rd ed., Springer Berlin Heidelberg, Berlin, Heidelberg, 2007, http://link.springer.com/10.1007/978-3-540-68888-4.
[47] S.R. More, Aircraft Noise Characteristics and Metrics, Technical Report PARTNER-COE-2011-004, Partnership for Air Transportation Noise and Emissions Reduction, 2011, https://rosap.ntl.bts.gov/view/dot/66406.
[48] J. Larminie, J. Lowry, Electric Vehicle Technology Explained, Wiley, 2012.
[49] B. Magliozzi, D. Hanson, R. Amiet, Propeller and propfan noise, in: H. Hubbard (Ed.), Aeroacoustics of Flight Vehicles: Theory and Practice, Volume 1: Noise Sources, National Aeronautics and Space Administration (NASA), VA, USA, 1991, https://ntrs.nasa.gov/citations/19920001380, NASA-RP-1258-Vol-1.